May 2005

Local Phenomena in Oxides by Advanced Scanning Probe Microscopy

Sergei V. Kalinin
Oak Ridge National Laboratory

Rui Shao
University of Pennsylvania

Dawn A. Bonnell
University of Pennsylvania, bonnell@lrsm.upenn.edu

Local Phenomena in Oxides by Advanced Scanning Probe Microscopy

Abstract
In the last two decades, scanning probe microscopies (SPMs) have become the primary tool for addressing structure and electronic, mechanical, optical, and transport phenomena on the nanometer and atomic scales. Here, we summarize basic principles of SPM as applied for oxide materials characterization and present recent advances in high-resolution imaging and local property measurements. The use of advanced SPM techniques for solutions of material related problems is illustrated on the examples of grain boundary transport in polycrystalline oxides and ferroelectric domain imaging and manipulation. Future prospects for SPM applications in materials science are discussed.

journal

J. Am. Ceram. Soc., 88 [5] 1077–1098 (2005)
DOI: 10.1111/j.1551-2916.2005.00383.x

Local Phenomena in Oxides by Advanced Scanning Probe Microscopy

Sergei V. Kalinin†

Condensed Matter Sciences Division, Oak Ridge National Laboratory, Oak Ridge, Tennessee 37831

Rui Shao and Dawn A. Bonnell†

Department of Materials Science and Engineering, University of Pennsylvania, Philadelphia, Pennsylvania 19104

In the last two decades, scanning probe microscopies (SPMs) have become the primary tool for addressing structure and electronic, mechanical, optical, and transport phenomena on the nanometer and atomic scales. Here, we summarize basic principles of SPM as applied for oxide materials characterization and present recent advances in high-resolution imaging and local property measurements. The use of advanced SPM techniques for solutions of material related problems is illustrated on the examples of grain boundary transport in polycrystalline oxides and ferroelectric domain imaging and manipulation. Future prospects for SPM applications in materials science are discussed.

I. Introduction

Recent advances in design and processing of complex materials raise new challenges in understanding structure and properties at very small length scales. While a number of techniques for structure characterization on length scales from atomic to macroscopic is available, probing local properties represents a more formidable challenge. Scanning probe microscopies (SPMs) offer direct, very often spectacular, views of local behavior in complex systems. The first use of SPM on oxides was the application of tunneling-based techniques on single crystals.[1,2] Over the last decade, SPM has become one of the primary tools in the characterization of single crystal, polycrystalline, and thin film ceramic materials. Variations of SPM have been used to examine surface topography in systematic studies of the thermodynamics of surfaces and interfaces (faceting, grooving, etc.),[3,4] roughness of fracture surfaces,[5] and morphological changes during chemical reactions and phase transitions.[6,7] The utility of local probes is illustrated by the fact that only 15 years after commercial SPMs became available, above 1750 papers per year[8] are published that cite scanning probes as a keyword. Several monographs have summarized the state of this field at various stages and books are available that provide introductions to the field and general overviews.[9–14]

Most applications utilize SPM as a straightforward qualitative mapping tool primarily for surface morphology measurements; however, several research groups interested in complex behavior of solids have examined fundamental tip–surface interactions and extended SPM to probe local electronic transport, dielectric, optical, ferroelectric, and magnetic properties. Rather than address all SPM approaches, this review will summarize recent advances in nanometer probes of complex properties, highlighting potential insights, as well as remaining challenges in the field. Applications to two classic materials problems in which local probes are playing a role in understanding fundamental behavior will then be presented: the effect of oxide grain boundaries on electronic transport, and ferroelectric domain interactions and dynamics in phase transitions, size effects, and fatigue.

(1) Cantilever-Based SPM

The first cantilever probe, atomic force microscopy (AFM), is based on Van der Waals interactions between a small, often atomically sharp, tip and a sample surface.[15] The micromachined cantilever combined with an optical, capacitive, or piezoresistive position detector serves as a force sensor that allows forces as small as 10^{-3} nN to be detected, providing the sensitivity sufficient to detect a single chemical bond or magnetic or electrical interactions at the nanometer level. The schematic force–distance relation shown in Fig. 1 illustrates that different interactions are expected, depending on the distance separating the sample and the tip. A rigorous description of these interactions involving realistic tip shapes and inhomogeneous surfaces is extremely complex, and additional interactions become involved at sample–tip separations under 2 nm. Some attempts have been made to treat several simplified cases theoretically.[16–19] Nevertheless, the simple relation in Eq. (1) can be used to describe AFM operation modes:

$$F_{\text{tip-surface}} = F_{\text{cb}} + F_{\text{VdW}} + F_{\text{el}} + F_{\text{magn}} \quad (1)$$

where F_{cb} are the forces due to chemical bonding between the tip and the surface, F_{VdW} are Van der Waals interactions, and F_{el} and F_{magn} are long-range electrostatic and magnetic forces, respectively.

D. W. Johnson, Jr.—contributing editor

Manuscript No. 20250. Received December 7, 2004; approved March 3, 2005.
†Author to whom correspondence should be addressed. e-mail: sergei2@ornl.gov; bonnell@lrsm.upenn.edu

Feature

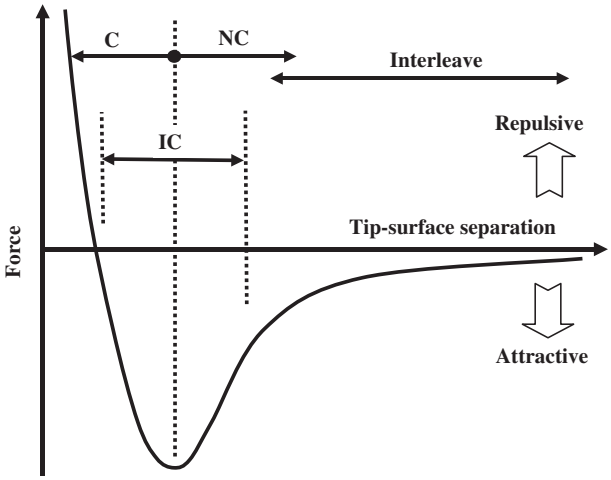

Fig. 1. A schematic of the dependence of force on sample tip separation showing the regimes in which contact (C), non-contact (NC), intermittent contact (IC), and interleave imaging are performed. Also shown are domains of repulsive and attractive tip–surface interactions.

At distances in the range of 1–500 nm the interaction is attractive; below 1 nm it becomes repulsive. The force is detected by monitoring the deflection of the cantilever on which the interacting tip is mounted. In contact mode, the interaction between the tip and the surface results in the deflection of the cantilever, which thus acts as a force sensor. A feedback loop keeps the static deflection constant by adjusting the vertical position of the cantilever base, providing a topographic image. In contact mode, i.e., imaging in the repulsive region of the Van der Waals forces, scanning can be destructive for both the tip and the surface. This limitation is circumvented in the intermittent contact mode AFM. Here, the tip is mechanically oscillated close to its resonance frequency. On approaching the surface, the oscillation amplitude decreases due to the interaction with the surface. The amplitude is then used as the detection signal and scanning is performed so that the oscillation amplitude is kept at predefined setpoint value smaller than the oscillation amplitude in free space. In intermittent contact mode, the tip interacts with the surface most strongly in the lower part of the trajectory. Finally, in non-contact AFM (NC-AFM), the tip oscillates in the attractive region of the Van der Waals forces and the resonant frequency shift of the cantilever measured by a phase lock loop is used as a feedback signal, providing the least invasive imaging.[20]

Atomic resolution[21] in contact mode AFM has been possible since the early 1990s, but in 1995 atomic resolution was demonstrated using NC-AFM.[22–24] There is an intrinsic tradeoff between spatial resolution and signal strength in AFM. Large oscillation amplitude optimizes the sensitivity in terms of signal to noise. High spatial resolution requires sample–tip separation on the order of several angstroms, limiting oscillation amplitude. In addition, the strong forces present in this regime can cause cantilever instability. Contrary to intuition, which suggested stiff cantilevers and small amplitudes, atomic resolution was achieved with relatively large amplitudes. Giessibl[22] has overcome these obstacles by designing a vertical cantilever (tuning fork configuration) with a very large spring constant and operating in frequency modulation rather than amplitude modulation. Figure 2 illustrates two examples of NC-AFM at atomic resolution on semiconductor and oxide surfaces: the Si (111) 7×7 reconstruction, a standard calibration surface for high-resolution SPMs, and the $SrTiO_3$ (100) $(\sqrt{5} \times \sqrt{5})$-R26.6° reconstruction,[25] a prototype oxide perovskite surface. The image in Fig. 2(a) shows the 7×7 reconstruction of the Si (111) surface. The fast scan axis (acquisition rate 3.2 lines per second) was oriented horizontally. During scanning, tip changes caused variations in contrast and resolution. The Si image was acquired in a dynamic frequency modulation mode, where a piezoresistive cantilever made from Si with a stiffness of 17 N/m and resonance frequency of 114 224 Hz was oscillated at an amplitude of 34 nm. The attractive forces acting between the tip and sample caused the frequency to drop by 70 Hz, and the image was created by controlling the tip–sample distance such that the frequency shift was constant at −70 Hz ("topographic imaging mode"). Although not yet as routine as STM, atomic resolution has been accomplished on a number of surfaces, including oxides, halides, semiconductors, and organic films.[26–31] NC-AFM has the potential to play the same role for insulating compounds as has STM for semiconductors and metals, with the added potential to detect weak electrostatic and magnetic interactions due to the addition of force sensitivity.

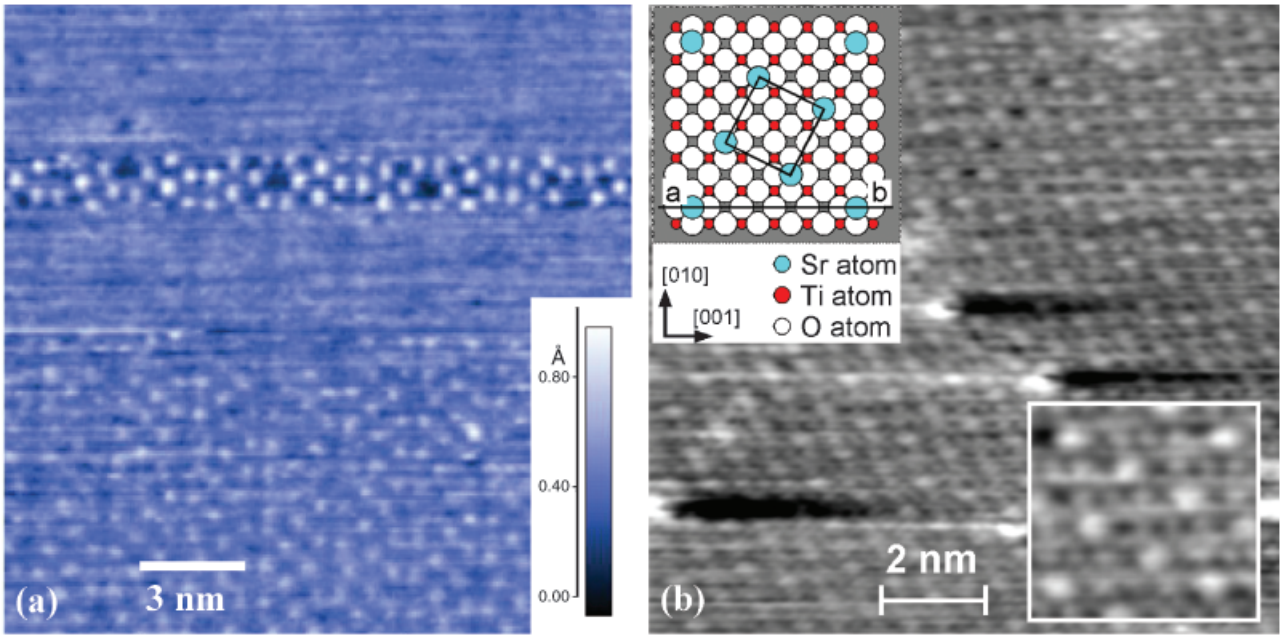

Fig. 2. (a) Atomic resolution NC AFM, Si (111) (7×7) imaged with a piezoresistive cantilever made from Si (17 N/m) and a resonance frequency of 114 224 Hz, an amplitude 34 nm, and constant frequency shift −70 Hz. Reprinted with permission from *Science*, **267** [5194] 68 (1995). (b) Atomically resolved NC-AFM image $SrTiO_3$ (100) after heating to 1200°C for several seconds along with a proposed model of the $SrTiO_3$ (100)-$(\sqrt{5} \times \sqrt{5})$-R26.6° surface reconstruction. Reprinted with permission from *Phys. Rev. Lett.*, **86,** 1801 (2001).

Sidebar 1: Long-Range Force Detection

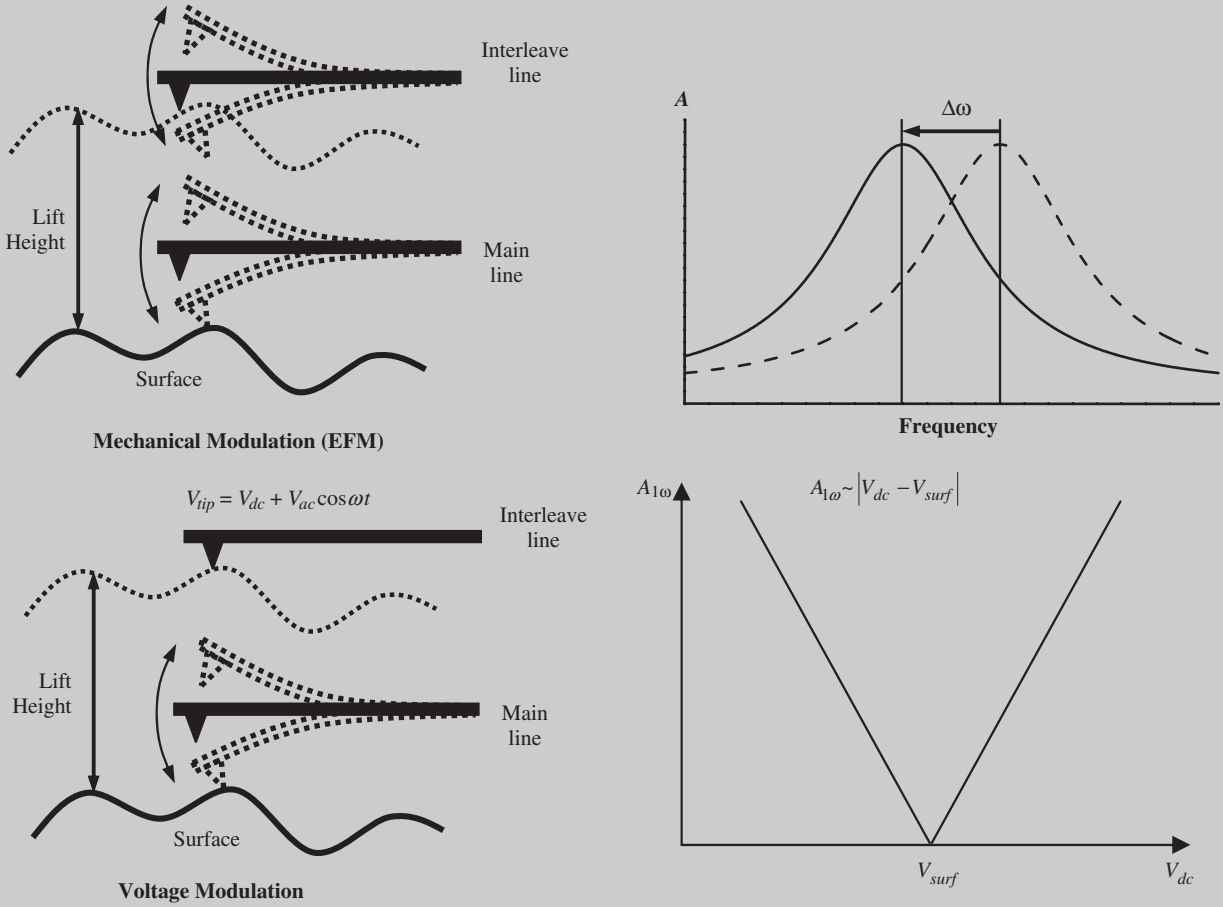

Electrostatic SPM techniques are based on the dynamic response of the probe to a mechanical or voltage modulation. These techniques are usually implemented in the lift mode. The tip first acquires the surface topography using standard intermittent contact AFM. Electrostatic data are collected in the second scan, during which the tip retraces the topographic profile with constant tip–sample separation.

In the mechanically driven mode, actuator induces cantilever oscillations and the tip-surface separation is $d = d_0 + A(\omega_p)\sin(\omega_p t + \varphi_c)$, where $A(\omega_p)$ is the frequency-dependent oscillation amplitude and φ_c is the phase shift between the driving function and the cantilever oscillations. The force gradient acting on the cantilever is detected through the resonant frequency shift (frequency detection) using the external phase locked loop electronics, or directly by amplitude, $A(\omega_p)$, or phase, φ_c, shifts. In the case of electrostatic force microscopy (EFM), the sensitivity to electrostatic field is enabled by using the biased tip for which $F \sim (V_{tip} - V_{surf})^2$. Measuring electrostatic force gradient signal allows mapping local surface potentials. However, interpretation of EFM is complicated by the fact that imaging is non-linear and strongly dependent on surface topography.

An alternative approach involves voltage modulation. The tip is not mechanically driven; rather, a conductive tip is biased by an AC voltage. In this regime, the piezoactuator is disengaged and an oscillating bias $V_{tip} = V_{dc} + V_{ac}\sin(\omega t)$ is applied to the tip during the lift mode scan. The first harmonic of capacitive force between the tip and the surface is

$$F_{1\omega}(z) = \frac{\partial C(z)}{\partial z}(V_{dc} - V_{surf})V_{ac}$$

where V_{surf} is the local surface potential. A feedback loop is employed to nullify $F_{1\omega}$ by adjusting V_{dc} on the tip. The condition $F_{1\omega} = 0$ is achieved when V_{dc} is equal to V_{surf}. Thus, the surface potential is directly measured by adjusting the potential offset on the tip and keeping the first harmonic response at zero. It is noteworthy that the signal is independent of the geometric properties of tip–surface system (i.e., $C(z)$) and the modulation voltage. This technique allows very high ($\sim$mV) potential resolution.

In addition to topographic sensitivity achieved through the Van der Waals force term in Eq. (1), SPM is also sensitive to electrostatic and magnetic interactions. At tip–sample separations on the order of 50–300 nm, the tip–surface interaction is dominated by long–range forces, such as those produced by electrostatic or magnetic fields. These force distributions can be isolated from topographic structure with the "lift mode" process outlined in Sidebar 1. Although there are challenges in quantifying images of complex inhomogeneous surfaces, e.g., in magnetic force microscopy and scanning surface potential microscopy, these have become common tools for mapping simple local properties. Currently, a wide range of more complex techniques are being developed to address elastic, linear, nonlinear, and frequency-dependent transport, electromechanical, optical, and other properties on the micro, nano-, and ultimately atomic scales. It is convenient to categorize scanning probe techniques in terms of tip–sample contact, source of cantilever oscillation, and feedback function, as shown in Fig. 3. Various scan-

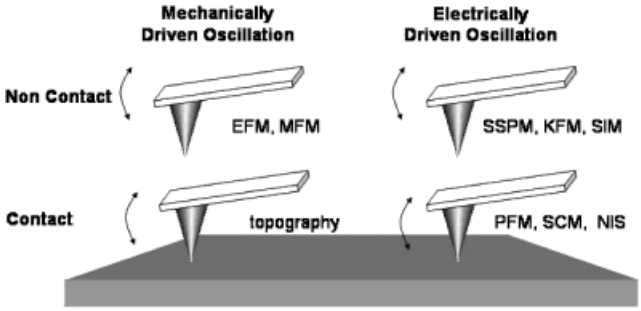

Fig. 3. Schematic representation of operational regimes for AFM. Techniques can be described as contact or non-contact with mechanically or electrically driven cantilever oscillation signals, resulting in four regimes in which most SPM techniques fall.

ning probe techniques are described in these terms in Table I, which also lists the properties that can be accessed with each. For example, conventional AFM can be a non-contact, mechanically driven oscillation with amplitude or phase-based detection. Piezoelectric force microscopy (PFM) is in contact mode, electrically driven with phase and amplitude-based detection. Combined with detection and/or feedback of not only first harmonic tip/surface response functions, but also second and third harmonic response functions, a wide range of properties can be accessed. An underlying theme of the newest developments is the use of multiple signal modulations or high-order harmonics of modulated signals. Within this framework, several techniques that address transport and dielectric properties will be reviewed.

(2) Advanced SPM Techniques for Transport Properties

Perhaps the most commonly used of the so-called "advanced" SPM techniques is scanning surface potential microscopy (SSPM), often referred to as Kelvin probe force microscopy (KPFM), which was developed to map the work function variation of a surface.[32,33] In SSPM, the cantilever oscillation is driven electrically, as described in Sidebar 1. This technique is implemented in lift mode with 50–200 nm probe–surface separation, and feedback on the first harmonic. The apparent ease with which potential variations can be mapped belies the challenges in interpreting images on electrically[34,35] and topographically[36] inhomogeneous surfaces. While for metallic surfaces the SSPM image can be represented as a weighted average of local potentials on the surface with the weighting factor given by a differential tip–surface capacitance gradient,[35] for semiconductor and dielectric surfaces the electrostatic properties are not characterized solely by intrinsic potential and topography. SSPM images of these surfaces should be interpreted in terms of *effective* surface potential that includes capacitive interactions, along with contributions from surface and volume bound charges, double layers, and remnant polarization.[37–40] For semiconductor surfaces without Fermi level pinning, tip-bias-induced band bending[41] can lead to a non-linear surface potential dependence on voltage,[42] further complicating quantification of experimental results.

Despite these challenges, the need to examine variations in local potential in electronic nanodevices spurred efforts to overcome some of the obstacles with careful analytical treatments that determined limits in quantification and allowed complex materials to be addressed. The late 1990s saw SSPM applied to semiconductor,[43,44] organic,[45] and ferroelectric[46,47] surfaces, as well as to defects,[48,49] and photoinduced[50,51]and thermal phenomena[52] in these materials. It is fair to say at this point that absolute values of potential cannot be quantified, but variations in potential can be determined with energy resolution of 2–4 meV and spatial resolution of the order of 50–100 nm.

Sensitivity of SSPM to local potential allows complex transport patterns in polycrystalline materials to be mapped. This is achieved by *in situ* measurements in which SSPM is performed while voltages are applied to and current is flowing through samples. These device configurations are often facilitated by microfabricated electrode arrays or electronic device test beds. SSPM detects local variations in surface potential, providing quantitative information on potential drops at each microstructural element. This approach is similar to the conventional four-probe transport measurements with the SPM tip acting as a moving voltage sensor, providing the advantage of spatial resolution. The general framework for SSPM-based dc transport measurements and corresponding equivalent circuit are illustrated in Fig. 4.

SSPM imaging of lateral transport is illustrated in Fig. 5, which shows the behavior of a polycrystalline ZnO surface under different bias conditions. The topography contains features due to contaminants and inter- and intragranular pores. Unlike conventional current-based probes sensitive to electrostatic potential, force-based probes are sensitive to electrochemical potential, thus providing non-vanishing contrast even on grounded surfaces due to the work function variations between dissimilar materials. In the particular case of ZnO, the potential depressions seen in Fig. 5(b) are associated with Bi-rich spinel phase inclusions, as confirmed by energy-dispersive X-ray (EDX) imaging.[53] On application of a 5 V lateral bias, the potential drops at the grain boundaries become evident. The contrast inverts on application of a bias of opposite polarity. Thus, the behavior of individual grains and grain boundaries is distinguished and the voltage dependence of all microstructural constituents can be examined separately.[54]

Table I. Properties and Modulated Operation Modes of Scanning Probes

Technique	Mode	Property	References
AFM	nc/ic, mech, phase/amp	VdW interaction, topography	9–12
EFM	nc, mech, phase/amp	Electrostatic force	9–12
MFM	nc, mech, phase/amp	Magnetic force, current flow	9–12
SSPM (KPM)	nc, elec, first harmonic	Potential, work function, adsorbate enthalpy/entropy	9–12,32–52
SCM	c, F, cap sensor	Capacitance, relative dopant density	9–12,56,59–66
*S*SRM	c, F, dc current	Resistivity, relative dopant density	9–12,56–58,62
SGM	nc, elec, amp	Current flow, local band energy, contact potential variation	9–12,72
SIM	nc, elec, phase/amp	Interface potential, capacitance, time constant, local band energy, potential, current flow (in comb. w/SSPM)	68–72
NIM	c, F, freq spectrum	Interface potential, capacitance, time constant, dopant profiling	74–76
PFM	c, elec, phase/amp	Piezoelectric constants d_{33} and d_{15}	2–5,78–93
SH-PFM	c, elec, second harmonic	Switching dynamics relaxation time and domain nucleation	106
SNDM	c, F, first or third harmonic	dC/dV, dielectric constant	110,111
NFMM	c, F, phase	Microwave losses	112–114

nc, non-contact; ic, intermittent contact; mech, mechanical; amp, amplitude; elec, electrical; c, contact mode; cap, capacitance; F, constant force feedback.

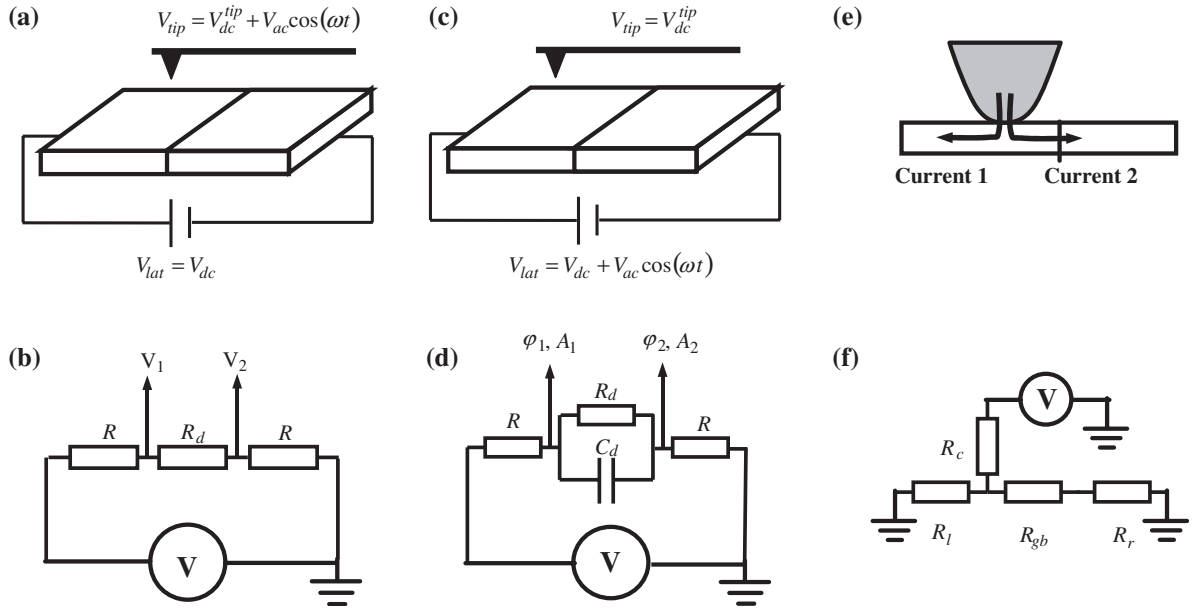

Fig. 4. Static- and frequency-dependent SPM-based transport measurements with (a–d) force- and (e,f) current detection. Shown is a schematic diagram (a,c,e) and corresponding equivalent circuit (b,d,f) of scanning surface potential microscopy (a,b), scanning impedance microscopy (c,d) and conductive AFM (c-AFM) (e,f). Note that c-AFM can also be configured as potential measurement technique by nulling tip–surface current (scanning potentiometry). However, the information in SSPM and SP is complementary–the former measures electrochemical potential, the latter electrostatic potential. Reprinted with permission from *Phys. Rev. B*, **70,** 235304 (2004).

The ultimate task of SPM-based dc transport measurements is the unambiguous determination of current–voltage (*I–V*) characteristics of individual microstructural elements from SPM images or spectroscopic data. For simple geometries (e.g., 1D nanotubes and oxide nanowires) in which current flow is uniform, the combination of SSPM under lateral bias with macroscopic current voltage measurements directly provides *I–V* characteristics of individual microstructural elements, the ultimate transport measurement tool. In more complex 2D and 3D systems, quantitative data analysis requires development of numerical image simulation tools, e.g., based on multigrid optimization methods.[55]

The primary limitation of SSPM for spatially resolved transport measurements is the slow response time of the feedback loop (~10 ms), which limits it to dc transport properties; approaches to extend SPM for frequency-dependent transport measurements are discussed below. Secondly, the typical spatial resolution of the order of 100 nm, while surpassing by several orders of magnitude conventional transport measurements, is still well below the nanometer level resolution common to many

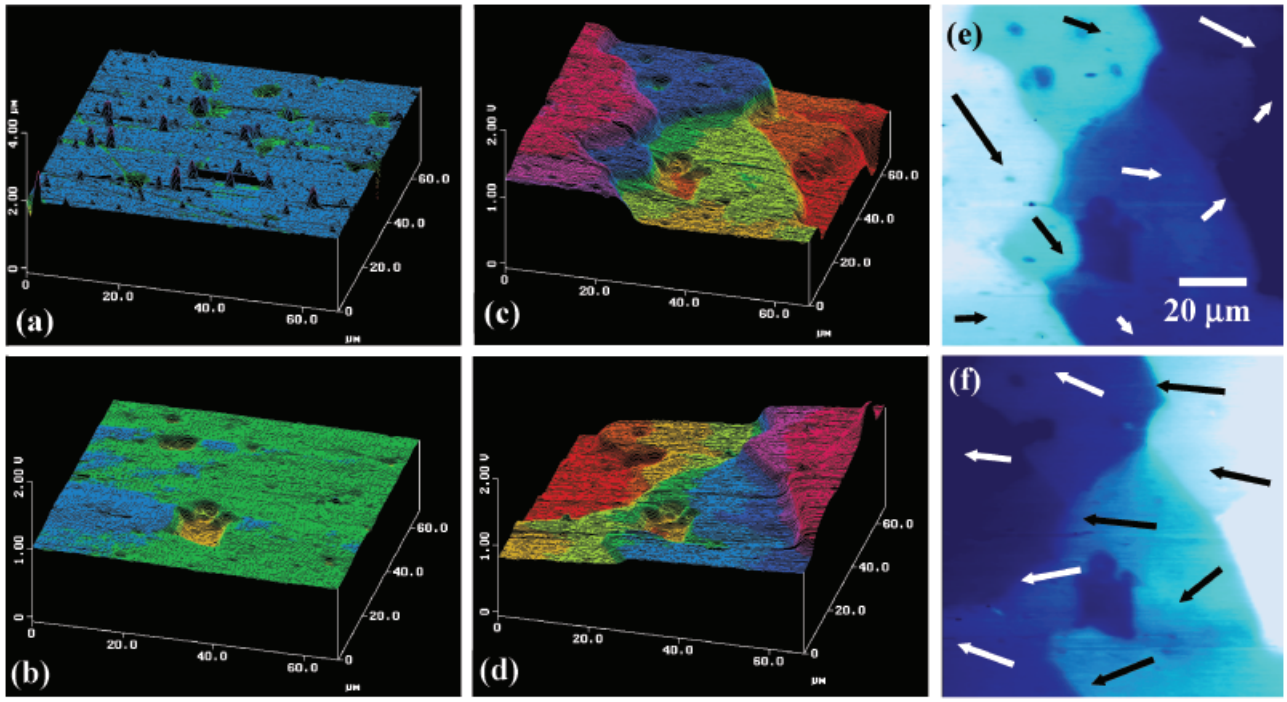

Fig. 5. Transport imaging in polycrystalline ZnO. (a) Surface topography. (b) SSPM image on a grounded surface shows local work-function variations due to Bi-rich spinel phase inclusions. (c,d) SSPM images under lateral bias exhibit potential drops at grain boundaries, indicative of grain boundary resistive behavior. Note that the direction of potential drops inverts with bias. (e,f) Current maps for positive and negative bias polarity.

topographic SPM techniques. This is a consequence of the fact that the imaging mechanism is based on capacitive interactions between the tip and the surface, in which a significant fraction of the tip contributes to the tip–surface force. This limitation can be circumvented by current-based contact mode techniques, in which tip–surface current, and hence resolution, are confined to the tip–surface contact area, typically of the order of several nanometers.

Two contact techniques, scanning spreading resistance microscopy (SSRM)[56–58] and scanning capacitance microscopy (SCM),[56,59–61] have been developed to address local resistance and non-linear capacitance. In SSRM, a conducting tip is biased with respect to a semiconducting sample and the dc current through the tip/surface contact is detected under force feedback control. The amount of current is determined from the spreading resistance of the surface, which is related to the local conductivity. Profiling usually requires a tip coated with a hard material (e.g. doped diamond) and a high spring constant cantilever to provide strong indentation forces ($\sim$20 μN)[56,62]. In SCM, a high-frequency capacitance sensor detects the tip/sample capacitance as the tip is scanned across the sample. Since the absolute value of tip–surface contact capacitance is in the aF range and cannot be detected directly, differential detection is used. An AC voltage applied to the tip induces the depletion and accumulation of carriers, resulting in a change in capacitance, ΔC. In a semiconductor, the depletion/accumulation width is inversely related to the carrier concentration, so mapping of $\Delta C/\Delta V$ yields the carrier concentration profile. Difficulties in quantification arise if the dopant concentration is non-uniform, and when spatial resolution decreases due to low dopant concentrations. A recent modification incorporates an additional feedback that adjusts ΔV to maintain a constant ΔC during the scan, maintaining a constant depletion width. Analysis of SCM results are mathematically challenging, usually requiring 2D or 3D numerical approaches.[63–66] While these have been applied primarily to semiconductors, they are equally applicable to conducting oxides.

SSRM and SCM provide complementary information about materials properties. For semiconductors, both techniques map carrier concentration, from which dopant concentration can be calculated, since both $\Delta C/\Delta V$ measured in SCM and spreading resistance measured in SSRM are directly related to carrier concentration. Both techniques yield zero signals on linear dielectric materials. SCM also provides a zero signal on metallic surfaces, while SSRM provides a strong signal on metals. SSRM is also insensitive to dielectric constant non-linearities, whereas SCM can be used for imaging non-linear dielectric materials, e.g., ferroelectric domain structures.

SSRM and its modifications, such as conductive AFM (c-AFM), can be used to map lateral transport in oxide materials. In conventional SSRM, tip–surface resistance is determined from the spreading resistance of material below the tip, thus accessing a small sample volume in the vicinity of tip–surface junction. Alternatively, the tip-induced current can be measured in the configuration illustrated in Figs. 4(e) and (f), where measured current or resistance between the tip and electrode provides information on both tip–surface junction and electroactive elements in the current path. Either the grain-boundary or the tip–surface resistance will dominate the image. Alternatively, c-AFM can be configured in the scanning potentiometry (SP) setup, in which lateral current is applied across the surface and tip–surface current is nullified by adjusting the tip bias similar to conventional potential measurements. Both SSPM and SP provide information about lateral transport in complex materials. The differences between these techniques are in terms of measured signal, resolution, and sensitivity to surface states. SSPM measures local electrochemical potential and, consequently, is sensitive to variations in surface composition; electrostatic potential can be obtained by subtracting potential images obtained on biased and grounded surfaces. With $\sim$100 nm lateral resolution SSPM is fairly insensitive to surface conditions and sample conductivity since force-sensitive imaging is performed with very high (>10 GΩ) tip–surface impedances. In contrast, SP measures electrostatic potential and resolution is limited by the tip–surface contact area and can be as small as several nanometers. However, SP and c-AFM require that tip–surface junction impedance be significantly smaller than the input impedance of the voltmeter and the impedance of other electroactive elements (e.g. grain boundaries), limiting these techniques to conductive ($\sim 1\ \Omega \cdot$cm) materials.

In order to explore mechanisms of transport in complex devices, it is necessary to determine frequency- and voltage-dependent responses. In macroscopic systems this is done with frequency-dependent perturbations or fast probes of relaxation from excited states. For example, the use of impedance spectroscopy based on the linear analysis of frequency-dependent impedance allows equivalent circuit descriptions corresponding to dominant relaxation processes to be modeled.[67] However, the generic limitation of all macroscopic techniques is that average transport properties are determined. Impedance spectroscopy allows the average interface resistance and capacitance to be measured and distinguished from the grain bulk or contact responses; however, it does not allow the responses of individual interfaces to be addressed. The first introduction of frequency dependence in transport scanning probes is referred to as scanning impedance microscopy (SIM).[68] This is a non-contact, first harmonic detection in which the oscillating electrical signal is applied to the sample instead of the tip (Sidebar 2). The tip can act as a non-perturbing probe in a configuration that allows both the amplitude and phase of local potential oscillations to be measured. Both resistive and capacitive elements of equivalent circuits are correlated with individual microstructural features, as illustrated in Figs. 4(c) and (d).[69] Alternatively, the biased tip in SIM can also act as a moving local gate, perturbing the current transport path.[70,71] Simultaneous SIM and scanning gate microscopy (SGM) imaging allows significant enhancement of the resolution in e.g. transport of carbon nanotubes.[72] The frequency dependence can be used to isolate relaxations associated with electron traps at interfaces and defects.

Figure 6 illustrates SIM measurements of spatially resolved phase angle and frequency dependence expected for a defect such as an interface or grain boundary. For a prototypical bicrystal sample, a circuit comprised of a single electroactive interface with resistance, R_d, and capacitance, C_d, in series with two current limiting resistors, R, the phase shift across the interface is

$$\tan(\varphi_d) = \frac{\omega C_d R_d^2}{(R + R_d) + R\omega^2 C_d^2 R_d^2} \quad (2)$$

where $\omega = 2\pi f$ and f is the linear oscillation frequency. Fitting the experimental interface phase shift determines interface properties similar to conventional impedance spectroscopy. For high frequencies, $\omega \gg 1/C_d R_d$, interface phase shift has the simple form $\tan(\varphi_d) = 1/\omega C_d R$ and interface capacitance can be calculated directly from the frequency shift. At low frequencies, the amplitude ratio across the interface, $A_1/A_2 = (R + R_{gb})/R$, is determined by a simple voltage divider effect.

A dc potential can be applied across the surface establishing a potential drop across the interface, which can then be measured by SSPM, while SIM is used to measure bias-dependent interface capacitance. Thus, the combination of the two techniques allows local transport spectroscopy of individual interfaces, e.g., direct measurement of the interface C–V characteristics. The quantitative nature of this approach has been confirmed on studies of Si/metal diodes.[73] Application of SIM for quantification of electronic transport in oxide materials is illustrated in Fig. 6, which shows the surface topography and phase shift across a $SrTiO_3$ bicrystal grain boundary, as well as the frequency dependence of interface phase shift for different circuit termination resistors, R. Solid curves are fits of experimental data using a simple R_{gb}–C_{gb}–R model. Interface resistance, R_{gb}, and capacitance, C_{gb}, were used to calculate the frequency de-

Sidebar 2: Scanning Impedance Microscopy

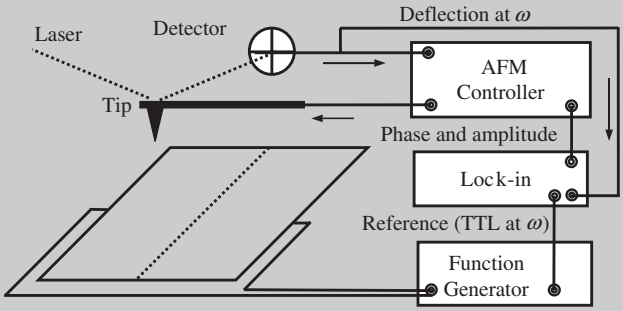

In SIM, the ac bias $V_{lat} = V_{dc} + V_{ac}\cos(\omega t)$ is applied across the surface. The lateral bias induces an oscillation in surface potential $V_{surf} = V_s + V_{ac}(x)\cos(\omega t + \varphi(x))$, where $\varphi(x)$ and $V_{ac}(x)$ are the position-dependent phase shift and voltage oscillation amplitude and V_S is the dc surface potential. Oscillation of the surface potential results in a periodic mechanical deflection on the cantilever. The variation of the phase (SIM phase image) provides the voltage phase variation along the surface since the phase lag is constant along the surface. At the same time, the tip oscillation amplitude (SIM amplitude image) is proportional to the local potential amplitude. The latter can be reconstructed using simple calibration procedure. This approach allows not only resistive, but also capacitive elements of the equivalent circuit to be measured.

pendence of the amplitude ratio, which is compared with experimental data in Fig. 6(d). Note the excellent agreement between the two despite the lack of free parameters, indicative of the self-consistency of the data.

Similar to SSPM, the spatial resolution in SIM is ultimately limited by the capacitive tip–surface interaction. In certain cases, the spatial resolution of SIM can be significantly enhanced if the measurements are performed under conditions when field-induced perturbations in the transport properties of the material are significant. SIM imaging in this "self-gating" regime allows direct insight into the characterized defect-mediated transport in a single carbon nanotube.[72]

The second approach to accessing frequency-dependent transport expands the frequency range to eight orders of magnitude and provides higher spatial resolution through the use of current, rather than force, detection. Nanoimpedance microscopy and spectroscopy (NIM)[74] is a contact probe with force feedback, in which the oscillating bias signal is applied to the tip. The phase and amplitude of the current through the tip–surface junction are detected as NIM images (Sidebar 3). This technique has rapidly gained popularity and has been used by several groups to study electrochemical behavior in a number of materials systems.[75,76] Figure 7 shows surface topography and NIM phase and magnitude images on ZnO surfaces illustrating the effects of second-phase inclusions on tip–surface impedance. Note that SIM and NIM provide complementary information on transport properties: SIM measures amplitude and phase of voltage oscillations along the surface induced by bias applied through external electrodes while the tip is a non-invasive probe; NIM measures the phase and amplitude of current generated in response to the tip bias and the tip is a part of an active current path.

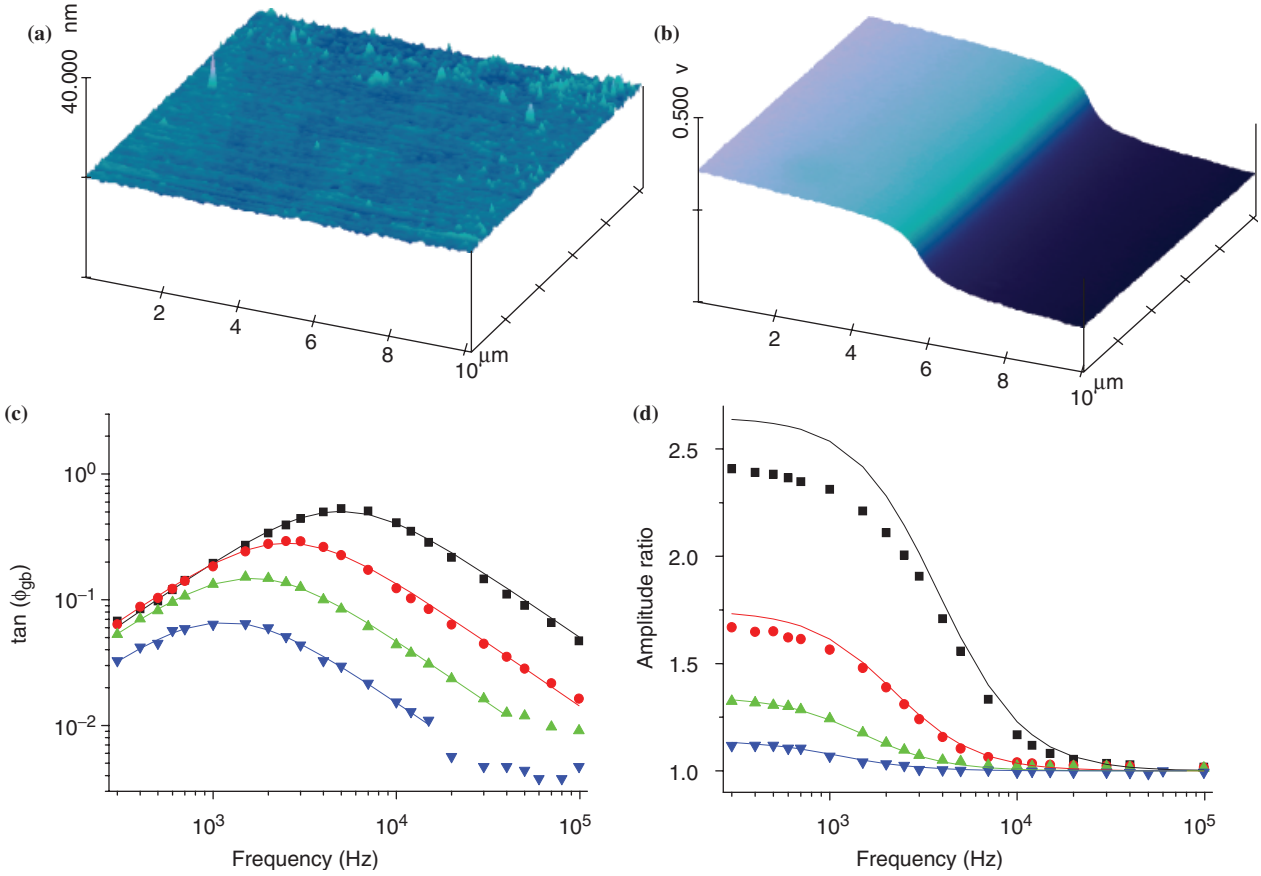

Fig. 6. Surface topography (a) and SIM phase image of a grain boundary in a Nb-doped Σ5 $SrTiO_3$ bicrystal. (c) Frequency dependence of SIM phase shift and (d) amplitude ratio. Solid lines on (c) are fits for frequency-independent grain boundary resistance and capacitance, on (d) calculations from using interface resistance and capacitance from phase data. Data are shown for circuit terminations 148 Ω (■), 520 Ω (●), 1.48 kΩ (▲), and 4.8 kΩ (▼). Reprinted with permission from *Phys. Rev. B*, **70,** 235304 (2004).

Sidebar 3: Nanoimpedance Microscopy and Spectroscopy

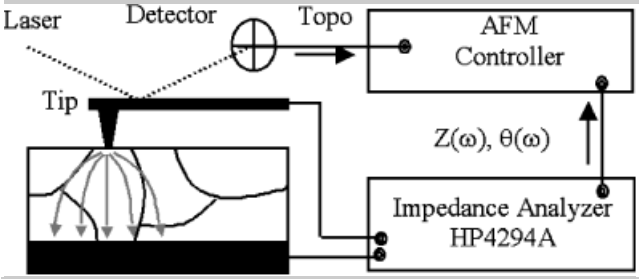

In NIM, AFM tip is connected as one terminal of the impedance analyzer. The second electrode is either bottom electrode (single terminal configuration), or micropatterned surface electrode (two-terminal configuration). NIM can be implemented in both imaging and spectroscopic modes. In the imaging mode, the tip acquires the surface topography in contact mode. A constant dc bias, V_{dc}, and a probing ac bias, V_{ac}, at frequency, f, is applied between the tip and the counter electrode. The impedance data at different tip locations are collected to form amplitude, $\ln|Z|$, and phase angle, θ, images, where measured impedance, $Z(\omega)$, is defined as the ratio of the probing voltage $V(\omega)$ to the measured current, $I(\omega)$, as $Z(\omega) = V(\omega)/I(\omega) = |Z|\exp(i\theta)$. In the spectroscopic mode, the tip position is fixed and the local impedance–frequency or impedance–dc bias spectra are acquired. Combination of this analysis with spatially resolved impedance imaging yields frequency, bias, and position-dependent information on microscopic transport properties.

Nanoimpedance spectroscopy is illustrated in Fig. 8 for a ZnO grain boundary. The electrode contact and grain boundary properties are distinguished as two semicircles in the impedance spectra, allowing the actual properties of the grain boundary to be characterized. The changes in grain boundary resistance and capacitance with tip bias are clearly seen, as indicated by shrinking of the Cole–Cole plots at higher biases. Alternatively, impedance–voltage data can be obtained at different locations along the surface, illustrating the impact of the grain boundaries between the tip and electrode on impedance spectra. The local boundary potential, capacitance, charge, and depletion lengths can be extracted with spatial resolution on the order of tens of nanometers. In a configuration with an electrode beneath the sample, the impedance of individual grains can be mapped, providing insight into grain-specific transport properties.

(3) Advanced SPM Techniques for Dielectric Properties

Utilizing higher-order harmonic signals and specialized detector design allows dielectric constant, electrostriction, and piezoelectric properties to be detected (Table I). Generally, the use of high-order signals is associated with an increase in spatial resolution due to the more rapid decay of the field with separation from the tip. A number of probes has been developed to quantify linear and non-linear dielectric properties locally. These have focused on electromechanical coupling coefficients, hysteretic ferroelectric domain switching, non-linear dielectric constant, etc.

Piezoresponse force microscopy (PFM), a scanning probe that holds the promise of determining electromechanical coupling coefficients at nanometer scales, is becoming an increasingly popular tool for the characterization of ferroelectric and piezoelectric materials.[77] PFM is a contact, electrically driven probe technique using standard contact mode AFM feedback for topographic tracing. The application of ac bias, $V_{tip} = V_{dc} + V_{ac}\cos\omega t$, to the tip induces an oscillating electrical field in the material. If the material is piezoelectric, the field results in a local deformation of the surface, $d = A_{1\omega}\cos(\omega t + \delta)$, that oscillates the tip, i.e. piezoresponse (PR).[78,79] This deformation can be related to the piezoelectric coefficients that characterizes electromechanical coupling in the lattice. The schematics of PFM and techniques for imaging local elastic properties such as atomic force acoustic microscopy (AFAM) and ultrasonic force microscopy (UFM) are illustrated in Sidebar 4.

The application of PFM that ensured its rapid popularity is nanoscale ferroelectric domain imaging. Domains with polarization vectors oriented downward contract with a positive voltage, producing a phase shift of $\delta = 180^\circ$. For upward oriented domains, the situation is reversed, and $\delta = 0^\circ$. The phase therefore indicates the orientation of atomic polarization. The piezoresponse amplitude, $A = A_{1\omega}/V_{ac}$, defines the local electromechanical activity of the surface.

Quantitative interpretation of PFM contrast is complicated by non-negligible electrostatic interactions between the tip and the surface, as well as between the cantilever and the surface so that the measured piezoresponse amplitude is $A = A_{el} + A_{piezo} + A_{nl}$, where A_{el} is the electrostatic contribution, A_{piezo} is the electromechanical contribution, and A_{nl} is the non-local contribution due to capacitive cantilever–surface interactions.[80,81] Quantitative PFM imaging requires that A_{piezo} be maximized to achieve predominantly electromechanical contrast. The cantilever size is usually significantly larger than the domain size; therefore, a non-local cantilever contribution is usually present in the form of an additive offset to the PFM image.

Even under optimal conditions, the origins of the electromechanical contribution, A_{piezo}, and its relationship to materials properties are not straightforward due to the complex geometry of the tip–surface junction. Some progress toward quantitative understanding of PFM has been achieved recently.[82–86] Depending on the tip size and indentation force, the PFM signal may correspond to the electromechanical response of the surface induced by the contact area (strong indentation limit) or be dominated by the electromechanical response of the surface due to the field produced by the spherical part of the tip (weak indentation limit). In these cases, the surface and tip displacement is determined by the electromechanical coupling in the material. Alternatively, the signal can be dominated by the electrostatic tip–surface interactions (electrostatic limit) that result in indentation even for non-piezoelectric materials. Quantitative measurement of the electromechanical properties of surfaces is possible only in the strong indentation limit, which (unfortunately) corresponds to a large tip–surface contact area. The measured piezoelectric response in this case is directly related to the piezoelectric constant tensor, d_{ij}, of the material. Taking an approach familiar to materials scientists, the analytical solutions of these interactions can be presented as contrast mechanism maps that relate experimental conditions to the properties of the material and delineate the conditions under which quantitative measurements can be obtained (Fig. 9).[87] This is critical since it has been shown that under some experimental conditions the response has no connection to local electromechanical properties.

In the strong indentation case where PFM image formation can be described using the indentation model, neglecting the effect of the part of the tip not in contact with the surface, the piezoresponse amplitude is determined in a complex manner by the complete set of piezoelectric, elastic, and dielectric constants of the material. Rigorously calculated PFM amplitude for the ideal case of a (100) surface of a tetragonal material was shown to be proportional to the piezoelectric coefficient, $A = \alpha d_{33}$, where α is proportionality coefficient close to unity.[88] This allows PFM image interpretation in terms of polarization orientation, since piezoelectric constant is related to the polarization magnitude as $d_{33} = \varepsilon\varepsilon_0 Q_{33} P$, where Q_{33} is electrostrictive coefficient.

The in-plane component of polarization can be accessed by measuring the lateral response of the tip.[89,90] The orientation

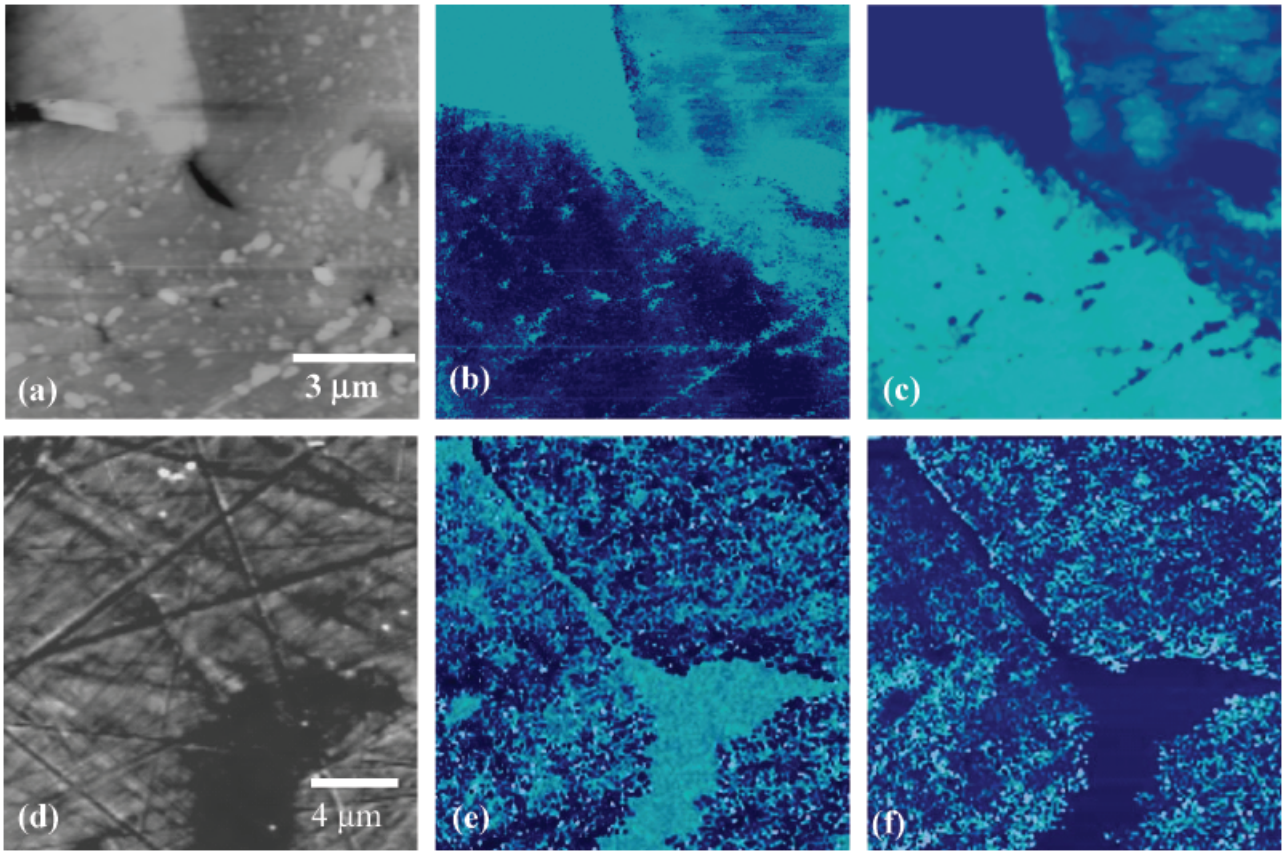

Fig. 7. Nanoimpedance microscopy (NIM) of polycrystalline ZnO ceramics. Surface topography images illustrate morphological features due to the Al_2O_3 grain embedded during polishing process (a) and due to the interface spinel-phase inclusion (d). NIM magnitude images (b,e) illustrate impedance mapping of the surface. Note that non-conductive inclusions are associated with impedance maxima. In (e), a non-conductive grain boundary layer can be clearly seen. (c,f) complementary NIM phase data. In non-conductive regions, tip–surface coupling is purely capacitive and $\theta = -90^\circ$. In conductive regions, the phase varies between $\theta = 0^\circ$ expected for purely resistive coupling and $\theta = -90^\circ$ for capacitive coupling. Quantitative analysis of magnitude and phase data at several frequencies provides information on local tip-surface resistance and capacitance. Reprinted with permission from *Appl. Phys. Lett.*, **82,** 1869 (2003).

dependence of the piezoresponse signal is a function of the angle between the surface normal and the polarization axis, the complexity of which depends on the symmetry of the compound and the orientation of the grain or crystal. Harnagea *et al.*[91] have shown that even for $BaTiO_3$ with relatively high symmetry it is not possible to deduce domain orientation from vertical PFM alone. Either the grain orientation or the in-plane component must also be known. The next step in ferroelectric imaging can

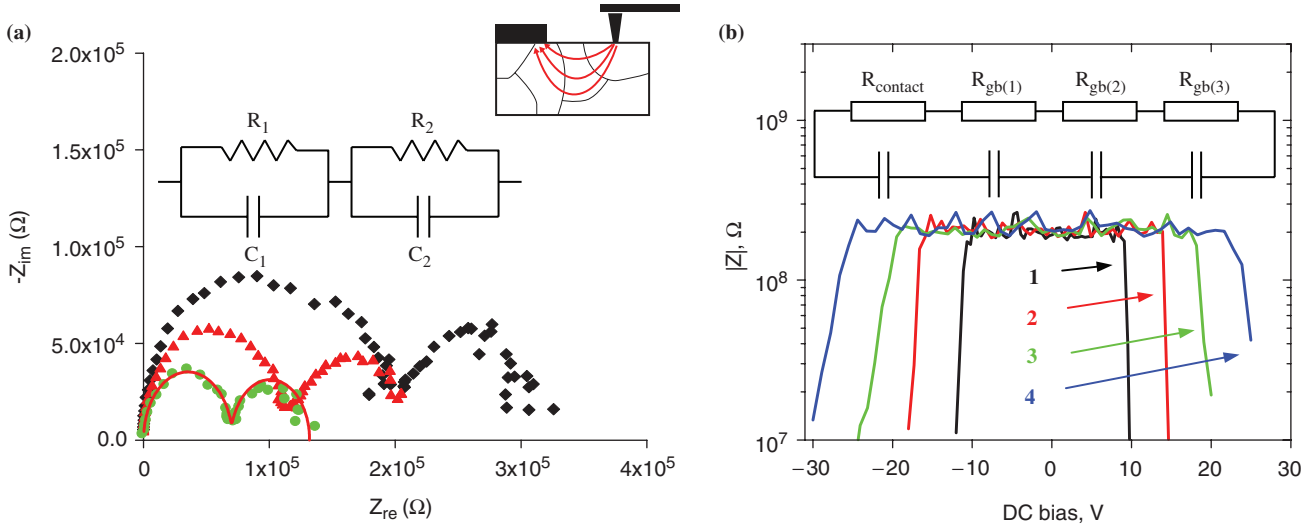

Fig. 8. (a) Cole–Cole plot of local impedance spectra between the SPM tip and the top electrode (nanoimpedance spectroscopy) at tip/sample biases of +5 V(●), +3 V(Δ), +2 V(◆) for a fixed tip location. The solid line is the fitting of impedance data to the equivalent circuit of two RC elements in series (—). Note that interface resistance decreases with dc bias, indicative of varistor behavior. (b) Bias dependence of tip-electrode impedance for different tip locations on the surface. Curves 1, 2, 3, and 4 correspond to transport through 1, 2, 3, and 4 grain boundaries, respectively. Partially reprinted with permission from *Appl. Phys. Lett.*, **82**, 1869 (2003).

Sidebar 4: Electromechanical and Elastic Measurements by SPM

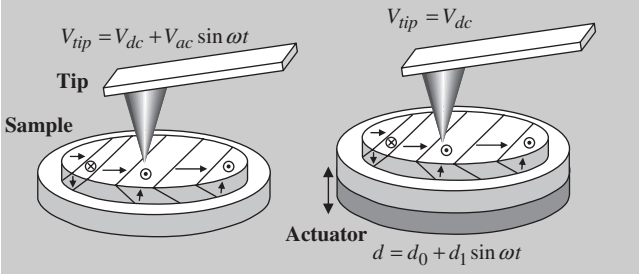

Piezoresponse Force Microscopy | **Atomic Force Acoustic Microscopy, Ultrasonic Force Microscopy**

In PFM, application of periodic bias, $V_{tip} = V_{dc} + V_{ac}\cos(\omega t)$, to the conductive tip in contact with ferroelectric surface results in periodic surface displacement, $d = A_{1\omega}\cos(\omega t + \theta)$ due to inverse piezoelectric effect. Mapping of the amplitude, $A_{1\omega}$, and phase, θ, of the displacement allows imaging of ferroelectric domain structures with ~3–10 nm resolution as described in the text. The vertical PFM (VPFM) is complemented by lateral PFM (LPFM) measuring the torsional component of tip vibrations, thus providing the information on the in-plane polarization component.

A number of SPM techniques based on mechanical phenomena such as AFAM [Rabe *et al.*, *J. Phys. D* **35**, 2621–35 (2002)] are developed to address the local elastic properties of the surface. Here, the sample is mounted on the piezoelectric actuator vibrating with the amplitude $d = d_0 + d_{1\omega}\sin(\omega t)$. This vibration amplitude is transmitted through the sample to the tip, vibration of which, $d_{tip}\sin(\omega t)$, is measured using standard optical detection. If the sample is hard (the spring constant of the tip-surface junction, k_{eff}, is much larger than the spring constant of the cantilever, $k_{eff} \gg k_s$), the vibration amplitude is transferred to the tip unattenuated, $d_{tip} = d_{1\omega}$. For soft materials ($k_{eff} \ll k_s$) the tip position does not change significantly, $d_{tip} \approx 0$. Thus, tip vibration amplitude provides information on the local elastic properties of materials. Measurement of associated phase distribution provides the information on the elastic losses inside the material, tip–surface junction and cantilever. In the high-frequency regime, the image formation mechanism in AFAM and related techniques such as UFM becomes more complex due to the dynamic stiffening of the cantilever.

be achieved by combining several lateral PFM images, which allows the construction of vector electromechanical maps.[92–94]

For materials with weak electromechanical coupling, bias-induced deflection can be below the noise level for the instrument, while the use of high modulation amplitudes can result in polarization switching below the tip. Recently, a number of approaches for using resonance-enhanced PFM was suggested to image polarization dynamics in materials with weak electromechanical coupling and close to phase transitions.[95,96] These advances have positioned PFM as one of the preferred methods of characterizing ferroelectric thin films and exploring the polarization dynamics on the nanoscale. Quantitative PFM measurements were used to address the depth dependence of ferroelectric properties in leveled thin film structures[97] and ferroelectric size effect in nanocrystals.[98,99] It has also been shown that mechanical strain produced by the tip can suppress local polarization[100] or induce local ferroelectroelastic polarization switching.[101–103]

The unique power of PFM is its potential for localized hysteresis loop measurements, i.e., PFM voltage spectroscopy, in which piezoresponse, $A_{1\omega}$, is measured as a function of dc potential offset, V_{dc}, on the tip.[90,104] PFM spectroscopy yields electromechanical hysteresis loops of individual grains, providing properties such as remanent response and coercive bias, on the ~50 nm level. PFM and spectroscopy of ferroelectric materials is illustrated in Fig. 10. Surface topography of the $PbTiO_3$ thin film with ~100 nm grains is illustrated in Fig. 10(a). Vertical and lateral PFM images shown in Figs. 10(b) and (c) illustrate the spatial distribution of electromechanical activity. Bright grains in the vertical PFM image correspond to grains with the polarization vector oriented upward, whereas dark grains correspond to grains with the polarization vector oriented downwards. Grains with intermediate contrast are either in-plane or non-ferroelectric. LPFM images provide information about the polarization orientation along the *y*-axis. Thus, the combination of VPFM and LPFM images determines two components of the polarization vector. For materials with a constant polarization magnitude, the third component can be deduced from these data. In the general case, however, LPFM after sample rotation or additional crystallographic data (e.g., electron back scattered diffraction or orientation imaging) are required. Figures 10(d) and (e) show vertical and lateral piezoresponse loops acquired on individual ferroelectric grains. These loops illustrate the critical tip bias required to achieve polarization switching and a number of attempts to relate local hysteresis with crystallographic orientation and piezoresponse amplitude have been reported.[105]

Further insight into local ferroelectric properties can be obtained from high-order PFM imaging. The relationship between higher order harmonics of the PR function and the time dependence of domain switching has been developed into a probe of switching dynamics in second harmonic piezoresponse force microscopy (SH-PFM).[106] When the field and the measured electrostrictive strain are in the *z*-direction, electrostriction is expressed in terms of the field-induced polarization, P, as $x = Q_{33}P^2$. For a ferroelectric with spontaneous polarization, P^S, and field-induced polarization, P^E, the strain becomes $x = Q_{33}(P^S)^2 + 2Q_{33}P^SP^E + (P^E)^2$, where the second and third terms are piezoelectric response (since $d_{33} = 2Q_{33}P^S/\varepsilon$) and electrostrictive response, respectively. On application of a small sinusoidal external field, $E_3(\omega) = E_3\cos\omega t$, induced polarization can be approximated as $P^E(\omega) = P^E\cos\omega t$ yielding

$$x = Q_{33}\left[(P^S)^2 + \frac{(P^E)^2}{2}\right] + 2Q_{33}P^SP^E\cos\omega t + \frac{1}{2}Q_{33} \times (P^E)^2\cos 2\omega t \quad (3)$$

In macroscopic measurements, electrostriction is quantified with interferometry.[107,108] In SH-PFM the cantilever oscillation in a contact mode SPM is used to determine local electrostrictive properties. Despite the fact that bias dependence of a first harmonic of the PFM signal has been interpreted as electrostrictive contribution, it was shown that the second harmonic signal on perovskites is primarily dominated by electrostatic tip–surface interactions. Direct detection of the second harmonic signal, and particularly observation of hysteresis loops, can unambiguously establish the presence of second-order ferroelectric effects.

Figure 11 shows the second harmonic hysteresis loop on polyvinilidendifluoride (PVDF). The signal is the reverse of the usual D–E hysteresis loop because the coefficient of the piezoelectric response $g_{33} = 2Q_{33}P^S$ corresponding to the first harmonic term in Eq. (3) is negative, since $Q_{33} < 0$ in this material.[109] Consequently, the PFM phase image of the upward domain created by poling with −10 V exhibits 0° phase shift and the negative domains exhibit 180° phase shift, in contrast to the behavior of oxide ferroelectrics. The first and the second harmonic responses, denoted by A_{1H} and A_{2H}, are shown in Figs. 11(d) and (e). A_{2H} versus V_{dc} also exhibits hysteretic behavior. More interestingly,

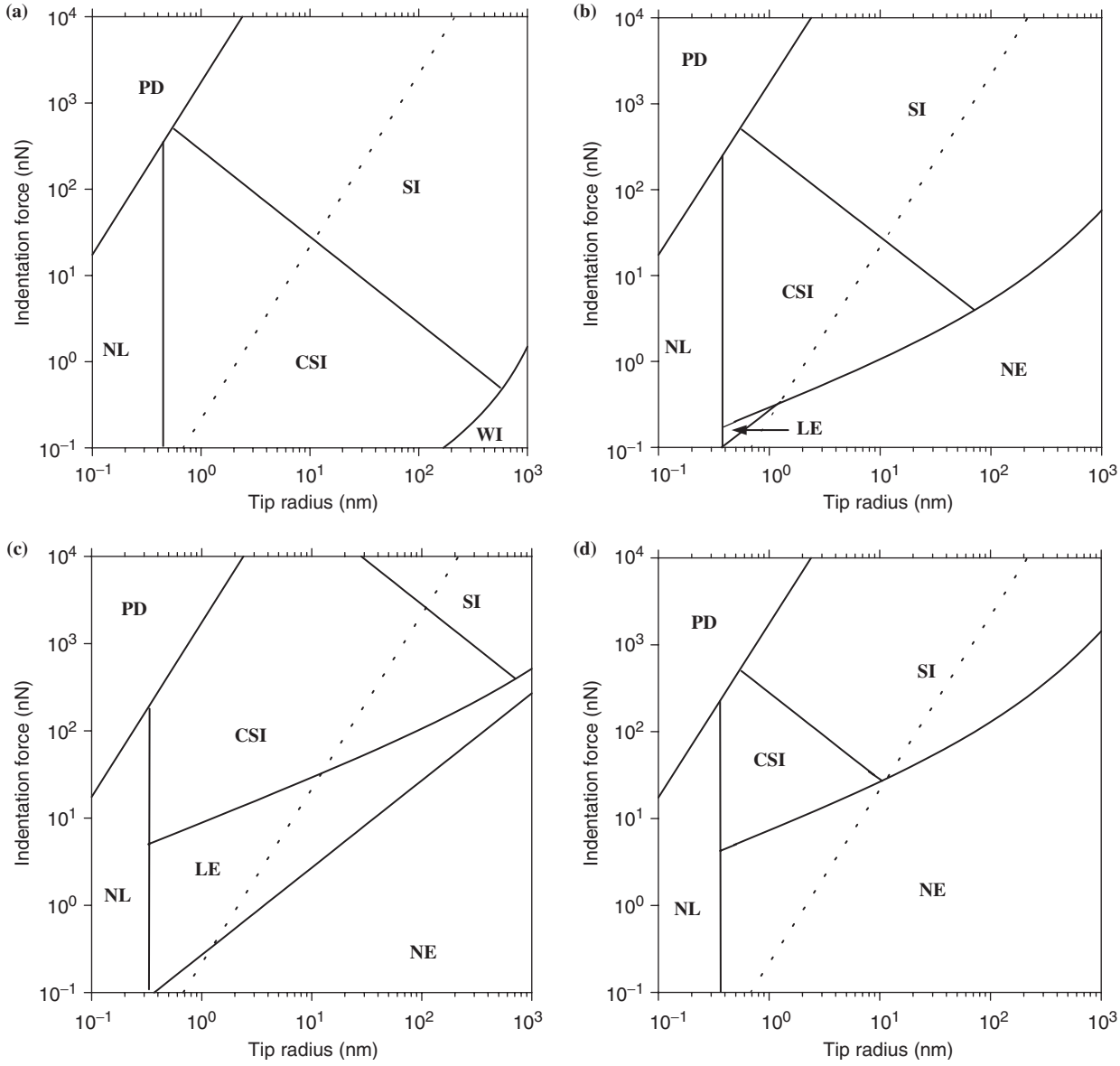

Fig. 9. Contrast mechanism maps of piezoresponse force microscopy. SI, strong indentation regime; CSI, contact limited strong indentation; WI, weak indentation regime; LE, linear electrostatic regime; NE, nonlinear electrostatic regime; NL. non-local interactions; PD, the plastic deformation. The dotted line delineates the region where stress-induced switching is possible. (a) $w = 0.1$ nm, $\Delta V = V_{tip} - V_s = 0$ V, (b) $w = 0.1$ nm, $\Delta V = 1$ V, (c) $w = 1$ nm, $\Delta V = 1$ V, (d) $w = 0.1$ nm, $\Delta V = 5$ V. Reprinted with permission from *Phys. Rev. B*, **65,** 125408 (2002).

during the ramping of V_{dc}, the first and second harmonic amplitudes follow opposite trends, i.e., when the former reaches maximum, the latter reaches minimum, and vice versa. A simple quantitative description of the first and second harmonics can be obtained in the limit that V_{ac} is small. In this case, V_{ac} can be seen as a small perturbation to V_{dc}, i.e. $V_{ac} = \mathrm{d}(V_{dc})$ and thus the V_{ac} induced P^E is $P^E = \mathrm{d}P^S/\mathrm{d}(V_{dc})\,\mathrm{d}(V_{dc})$. This yields $A_{1H} = 2|Q_{33}|P^S\,\mathrm{d}P^S/\mathrm{d}V\,\Delta V$, and $A_{2H} = |Q_{33}|(\mathrm{d}P^S/\mathrm{d}V\Delta V)^2$. The hysteresis in A_{2H} is in effect the dependence of the derivative dielectric constant ε on field, since $\mathrm{d}P^S/\mathrm{d}V = \mathrm{d}P^S/L\,\mathrm{d}E = \varepsilon/L$, where L is the thickness of the film. When V_{dc} is high, P^S becomes large but the corresponding ε becomes small. By comparing the contrast in the first and the second harmonic amplitude images (Figs. 11(b) and (c)) on the poled sample, several regions with bright contrast in Fig. 11(b) have dark contrast in Fig. 11(c) and vice versa. This phenomenon is the direct illustration of Eqs. (5) and (6). Furthermore, $(P^S)^2 = A_{1H}^2/4Q_{33}A_{2H}$. Thus the dielectric hysteresis loop P^S versus V_{dc} can be constructed if Q_{33} for this material is known. Conversely, Q_{33} is deduced from the local D–E hysteresis loop.

An alternative strategy to accessing linear and non-linear dielectric properties based on microwave–surface interactions is referred to as scanning non-linear dielectric microscopy (SNDM)[110,111] and near-field microwave microscopy (NFMM).[112,113] The approach utilizes a coaxial probe in which a sharp, center conductor "tip" protrudes. The probe serves as the end of a transmission line coupled with a resonator, which is coupled to a microwave source. In the configuration used in Anlage's group the probe tip is held fixed, while the sample is supported by a spring-loaded cantilever applying a controlled normal force on the order of 50 μN between the probe tip and the sample. The concentration of the microwave fields at the tip changes the boundary condition of the resonator, and, hence, the resonant frequency and quality factor. The magnitude of the perturbation depends on the dielectric properties of the sample. The spatial resolution of the microscope in this mode of operation is about 1 μm. NFMM has shown to be promising in mapping dielectric constant variations in a number of complex oxides, i.e., ferroelectric and superconducting compounds. Anlage *et al.* have demonstrated that high-order harmonic powers acquired by NFMM can be used to spatially resolve the local

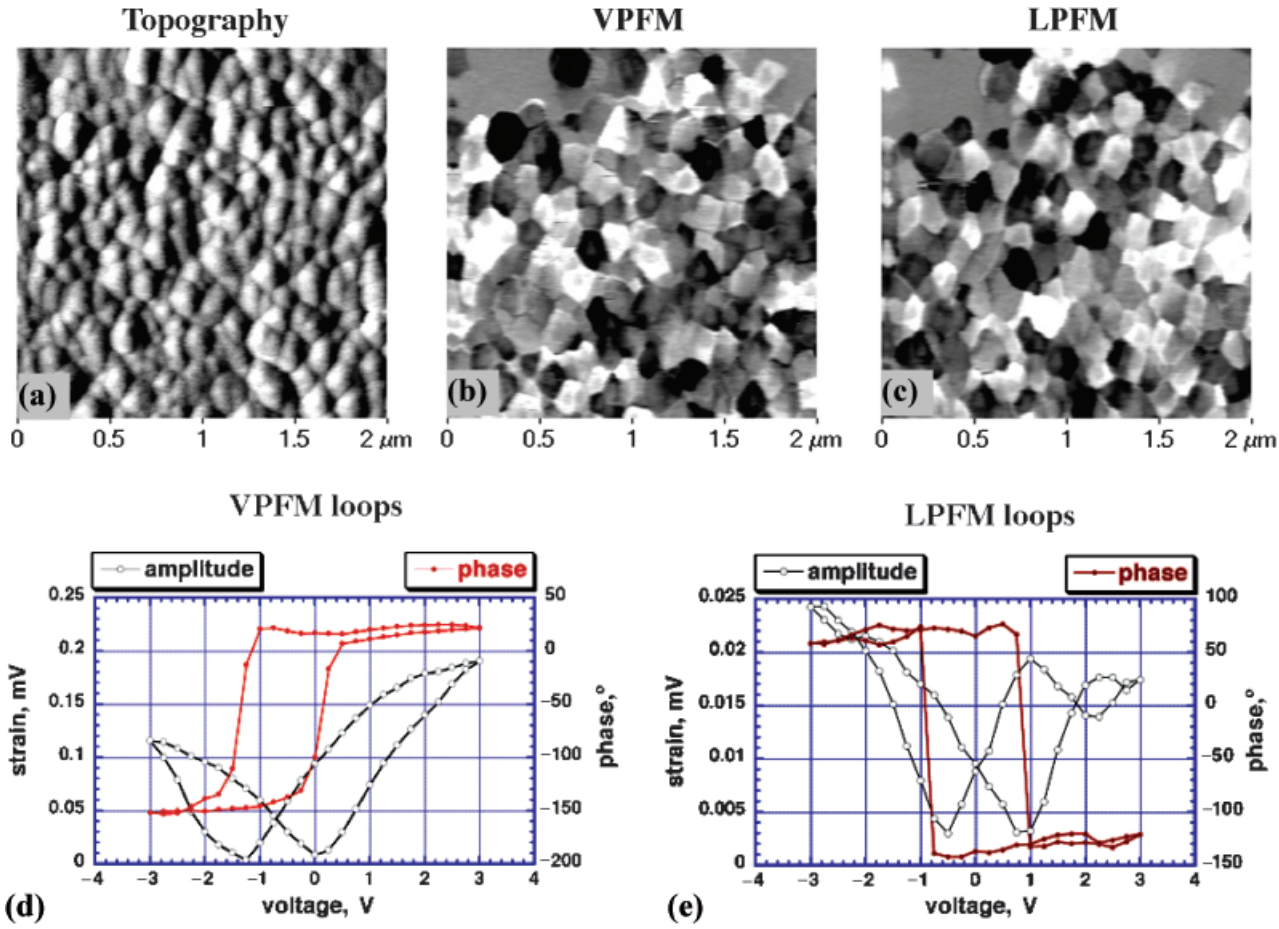

Fig. 10. Surface topography (a) and vertical (b) and lateral (c) PFM images of $PbTiO_3$ thin films. (e) Vertical and (f) lateral phase and amplitude hysteresis loops. Partially reprinted with permission from *J. Appl. Phys.*, **92,** 2734 (2002).

non-linearity. In their work, the grain boundary area of superconducting YBCO thin film deposited on a $SrTiO_3$ bicrystal was spatially resolved from the ratio of the second and the third harmonic responses.[114]

II. Local Probes Providing Insight into Classic Materials Issues

As noted above, scanning probes are becoming ubiquitous in condensed matter physics, solid state chemistry, biology, and several fields in engineering. The "advanced" techniques summarized here contribute considerable insight into two classic materials science problems: grain boundary structure/property relations and ferroelectric domain imaging and dynamics. These are longstanding areas of research interest in which fundamental understanding is being moved substantively forward by nanometer scale measurements of properties.

(1) Interface and Grain Boundary-Mediated Properties

One of the basic underpinnings of materials science is the role of grain boundaries in determining the properties of solids. The current and rather advanced understanding of this role is due, in a large part, to studies that relate interface atomic structure to behavior. Motivated by applications in the electronic ceramics industries, polycrystalline oxides have been the subject of study for over five decades. ZnO and titanates are often taken as model systems for transport-related properties and have been investigated by a range of macroscopic measurements including *I–V*, voltage-dependent capacitance, frequency-dependent impedance, etc.[115] Since macroscopic transport measurements access an ensemble of grains, these approaches yielded models of device behavior in terms of average grain and grain boundary properties. In these models the grain boundary acts as a potential barrier to electron transport, which is overcome by high voltages (varistor) or ferroelectric phase transformations (thermistor). This approach was sufficient to drive empirical optimization of materials but was less satisfying in elucidating fundamental behavior. This became even more troubling when high-resolution transmission electron microscopy (TEM), energy-dispersive spectroscopy, and Auger electron spectroscopy showed that grain boundary structure and composition vary widely in these materials.[116–119]

One approach to probing grain boundary behavior is to use local measurements in polycrystalline materials to isolate the behavior of individual boundaries. For example, scattering in scanning electron microscopy has been used to determine some aspects of grain boundary structures in polycrystalline ZnO, while conductive mode contrast yields some correlation to electronic properties.[120] Others have used cathodoluminescence and electron-beam-induced current methods to image variations in boundary properties.[121]

To specifically access individual boundaries, several groups use microfabrication techniques to pattern arrays of electrodes on a surface in such a way that individual boundaries are located between electrodes. Fleig *et al.*[122] have used impedance spectroscopy in this configuration to characterize transport properties of individual interfaces. Figure 5 of ZnO above shows how SSPM can be used to quantify inhomogeneous potential variations in polycrystalline materials *in situ*, i.e., with applied bias and current flowing through a device. In addition, the fact that the property information is digital allows mathematical analyses of the property data. In this case taking directional derivatives of the potential gradient allows the direction of current flow though an inhomogeneous media to be mapped.

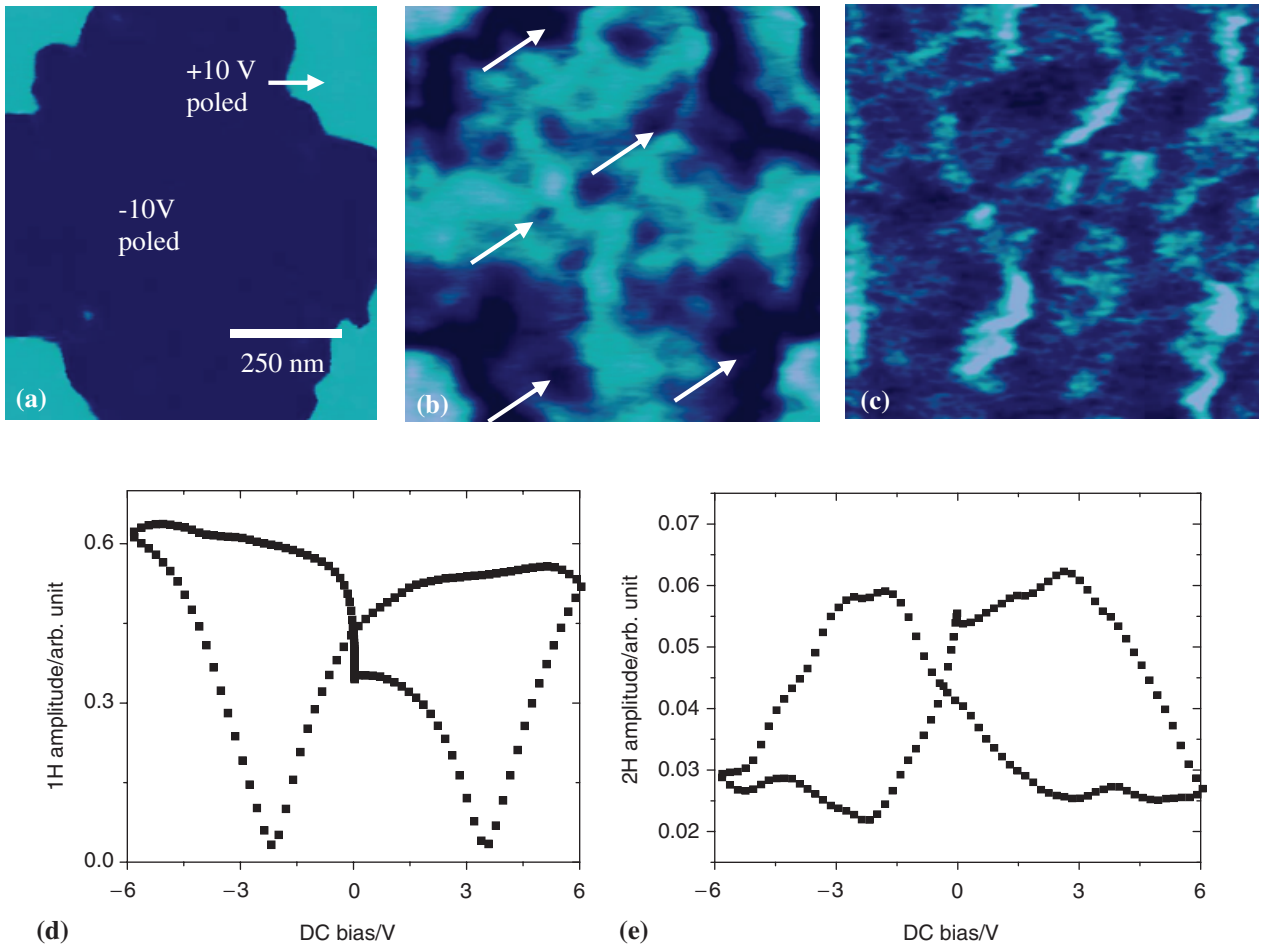

Fig. 11. (a) PFM phase image of poled polyvynilidenfluoride (PVDF) thin film. The upward domain poled with −10 V shows lower phase shift while negative domains poled with +10 V show higher phase shift. (b) Corresponding first harmonic amplitude image. (c) Second harmonic PFM amplitude image of the same region. First harmonic amplitude of P(VDF-TrFe) polymer thin film (a) and second harmonic amplitude (b) hysteresis loops showing opposite trend versus the external field. Arrows indicate the direction of change in V_{dc}. Reprinted with permission from *Jpn. J. Appl. Phys.*, **43,** 4471 (2004).

A recent study of $BiFeO_3$ presents an example of how multiple SPM techniques can be used to correlate microstructure with behavior in polycrystalline complex oxides.[69] Macroscopic impedance spectroscopy indicated the presence of a low-frequency RC (relaxation frequency 180 Hz) feature in polycrystalline $BiFeO_3$, which is both semiconducting and ferroelectric. SSPM performed at frequencies *below* the RC relaxation frequency and SIM performed at frequencies *above* the RC relaxation frequency were combined with AFM and PFM. The surface potential of grounded $BiFeO_3$ exhibited variations due to ferroelectric domains and surface contaminants. While the application of a 10 V lateral bias made the potential barriers at the grain boundaries evident, the potential features related to ferroelectric polarization were independent of the applied bias. Ramping the dc bias across the sample showed that the potential drop at the interface is linear in external bias and exhibits ohmic behavior for small biases ($\Delta V_{gb} < 50$ mV). The frequency-dependent SIM demonstrated well-defined phase shifts at the grain boundaries, while the amplitude displayed a uniform decrease across the surface. These observations identified the grain boundaries, rather than ferroelectric domain walls or electrode contacts, with the low-frequency relaxation process in the impedance spectrum.

A second approach to isolating grain boundaries is to produce model bicrystal interfaces. The first of these involved using Si bicrystal boundaries as models of semiconducting oxides. The seminal study by Pike and Seager[123] laid the groundwork for all subsequent investigations. In the last decade, the availability of high-quality $SrTiO_3$ bicrystal boundaries has enabled dramatic progress toward fundamental understanding. A community-wide effort has been undertaken to relate atomic structure at interfaces to properties,[124–136] and has motivated intensive theoretical studies.[137–139] Johnson and Dravid[129] used four-point probe transport measurements in parallel with high-resolution TEM and electron holography to characterize a 36.8° boundary in Nb-doped $SrTiO_3$ bicrystal. De Souza *et al.*[124] have determined the temperature and oxygen partial pressure dependence (room temperature and above) of impedance spectra of a 5.4° [001] tilt boundary in Fe-doped crystal and compared it to a structure determined from high-resolution TEM.

These studies have determined that the generalized structure of $SrTiO_3$ boundaries consists of pentagon-like structures containing two atomic columns. An example is shown in Fig. 12. The pentagons are formed on both the Sr and Ti–O sublattices with a double Sr column or a double Ti column in the middle. Some boundaries can be described completely with these pentagons and some require the addition of a heavily distorted unit cell-like structural unit between the pentagons. These relatively simple structures allow the atomic basis of local properties to be inferred. Recent studies of local oxidation state by electron energy loss spectroscopy (EELS) have shown that the electron density and dielectric properties at the grain boundary are different from those of the bulk.[127] At the limit of a low angle grain boundary the detailed structure has been elucidated. Zhang *et al.*[140] found that a $5^\circ\langle 100\rangle$ tilt boundary consists of a periodic array of a [100] dislocation. Using HRTEM and EELS they found that the dislocation cores are oxygen-deficient and reconstruct. They also found that the $\Sigma 3\,\{111\}\langle 110\rangle$ tilt boundary is oxygen deficient and relaxes.[141] It is usually assumed that the oxygen deficient structures result in a positive boundary charge

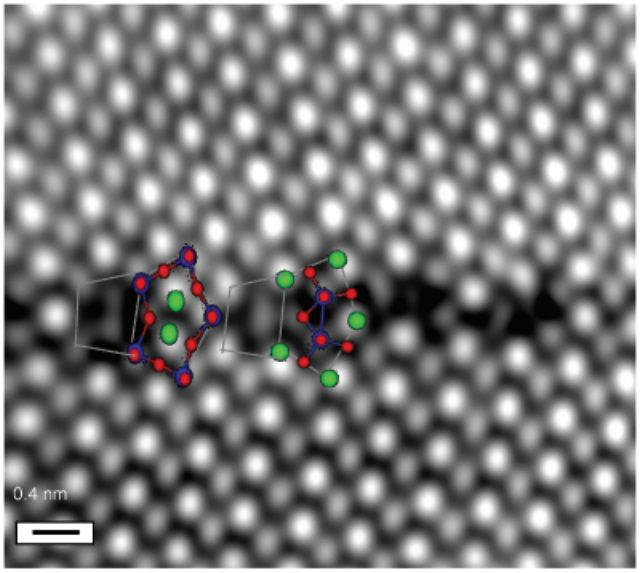

Fig. 12. Structural building blocks of $SrTiO_3$ grain boundaries. Z contrast image of a $SrTiO_3$ 24° bicrystal grain boundary. This structure consists of Sr and Ti containing pentagons with a separating unit cell in between. These relatively simple structures allow details of structure to be related to properties. (Image courtesy of G. Duscher and M. Chisholm, NCSU and ORNL.)

and electrical properties are described in terms of a negative space charge region. Many of these studies were done on acceptor-doped samples. It is not clear that the same can be said of donor-doped samples, in which mobile electrons might be trapped at oxygen vacancies, making the boundaries negative.

A variety of scanning probe measurements of $SrTiO_3$ bicrystals has elucidated local properties in the vicinity of the grain boundary. At the submicron level, McDaniel *et al.*[142] and McDaniel and Hsu[143] have used an advanced near-field optical microscopy technique to quantify strain around voids at these grain boundaries. They have added polarization modulation to transmission near-field scanning optical microscopy (NSOM). The approach yields birefringence and dichroism as well as transmission images. Cubic $SrTiO_3$ is optically isotropic with negligible absorption in the visible range. Strain fields alter the local refractive index and the first and second harmonics of the polarization modulated optical signal quantify strain. Figure 13 illustrates NSOM imaging of a 24° boundary. The voids beneath the surface are not evident in the topographic images but are clear in the transmission (b–d) optical images. The linear retardance image based on the first and second harmonic reveals isotropic contrast due to local strain. The maximum strain magnitude observed near voids in 24° boundaries was 0.021 and for 36° boundaries was 0.052.

Transport-related scanning probes such as SIM and NIM have recently revealed local property variation in the vicinity of grain boundaries associated with the structural perturbation of the grain boundaries: local dielectric constant variation[144] and interface-induced phase transformation.[145] These phenomena have been revealed by temperature-dependent transport measurements. The temperature dependence of interface capacitance and potential of a 36.8° boundary are compared to the temperature dependence of dielectric constant, Fig. 14. The temperature dependence of the grain boundary capacitance is significantly weaker than that of the bulk dielectric constant.

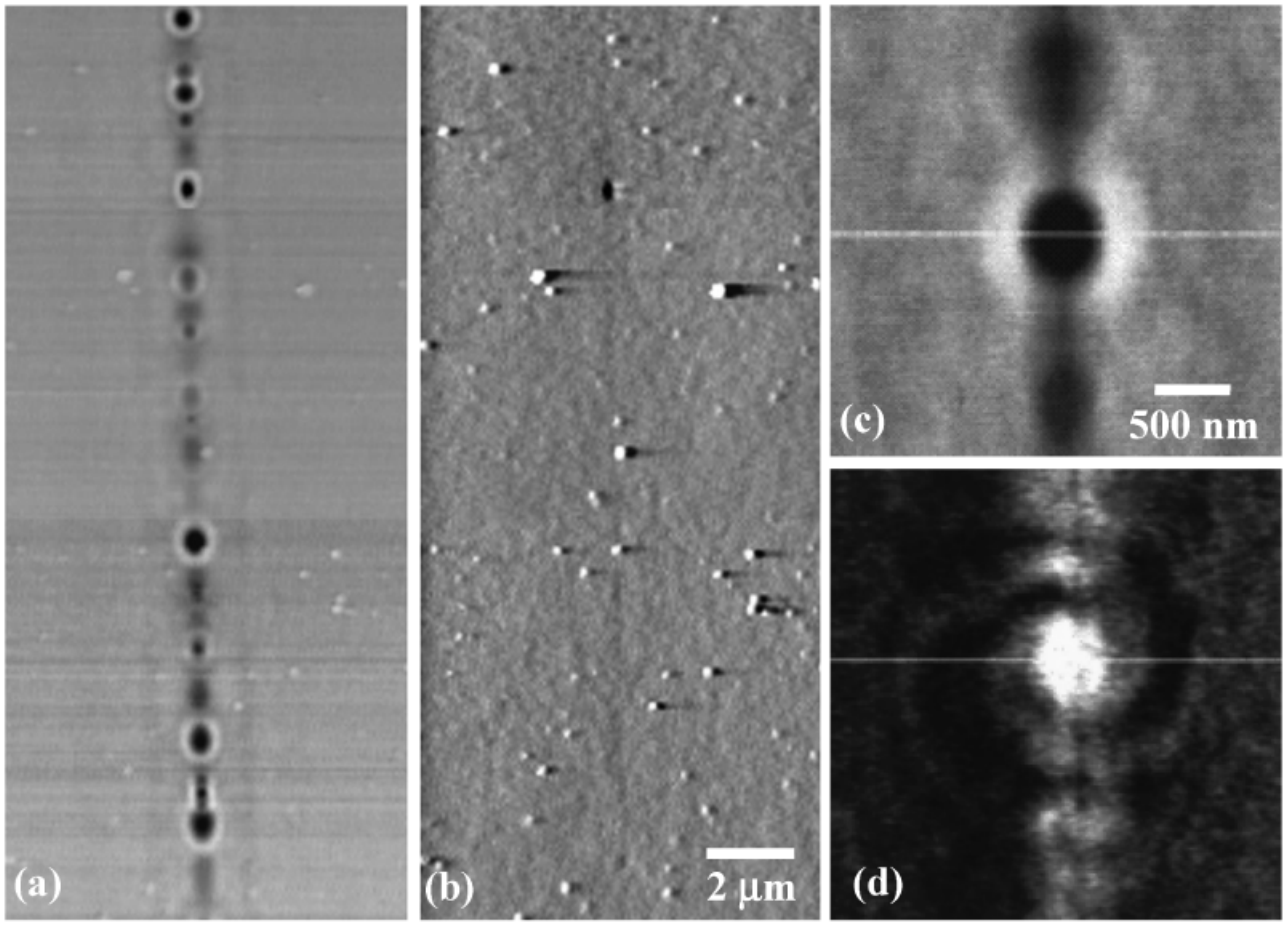

Fig. 13. Transmission and topographic images taken simultaneously on a 24° $SrTiO_3$ bicrystal. The gray scale represents 30% optical contrast in (a) and 3 nm height in (b). The transmission (c) and magnitude (d) of linear retardance image of a single defect show the oscillation of strain fields near the voids. The gray scale represents 0.05 rad (c). Reprinted with permission from *J. Appl. Phys.*, **84,** 189 (1998).

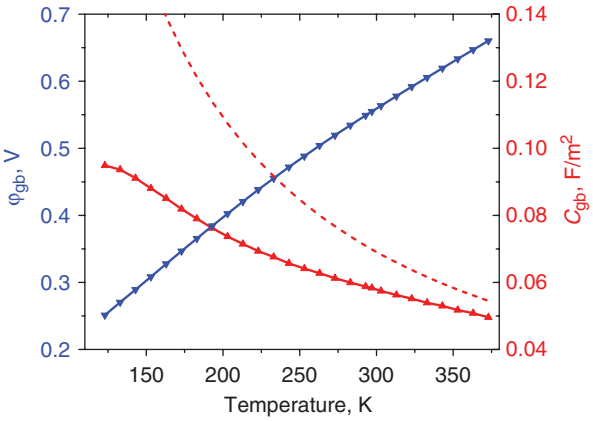

Fig. 14. Temperature dependence of interface potential barrier (▼) and interface capacitance (▲) of $SrTiO_3$ 36° grain boundary compared to the temperature dependence of dielectric constant (dashed line).

Independently fitting the temperature dependence of interface charge and interface capacitance allows the amount of local dielectric non-linearity to be quantified. The dielectric non-linearity required to explain the difference between the two curves is large and within a factor of 1.5–2.0 of that measured in thin films. The agreement in the magnitude of the dielectric non-linearity in the vicinity of the grain boundary determined from two different experimental measurements is strong support for the existence of dielectric constant variation near the interface. In this case, the perturbation in atomic structure that extends only 1 nm into the lattice establishes an electric field on the order of 10^8 V/m.

In the Nb-doped samples, a reversal in the temperature dependence of resistance at lower temperatures is observed.[145] In the entire temperature range, current–voltage relationships are non-linear for both 36° and 24° grain boundaries in Nb-doped samples, while the bulk conductance is ohmic. Since the bulk is several orders of magnitude more conducting than boundaries, its contribution is negligible. As the temperature decreases, the boundary resistances first increase, then drop by two orders of magnitude to a minimum around 30 K, and then slightly increase during further cooling to 1.4 K. This behavior resembles a PTCR transition and indeed there is a structural phase transition at 105–140 K. In bulk $SrTiO_3$, ferroelectric dipole coupling does not occur at this transition. The hypothesis is that the field associated with the boundary induces alignment of polarization vectors locally, thus compensating interface charge and reducing the resistance. If this proves correct, then these data represent a grain-boundary-induced phase transformation. In polycrystalline samples, Petzelt *et al.*[146] used Raman spectroscopy at the phase transition and indicated that the polarization vector is perpendicular to the tetragonal *c*-axis, which defines the direction of the tetragonal distortion with respect to the structure shown in Fig. 12. The grain boundary charge determined from transport measurements in both 24° and 36° boundaries in Nb-doped crystals is ~1 electron per Ti pentagon, a further indication of the structural origin.

A final note concerns results obtained using electrostatic-based SPMs on electrically inhomogeneous surfaces in air, of which a grain boundary is an example. It is obvious that atmospheric adsorbates can adsorb on any surface. In the case in which surface charge is inhomogeneous, the adsorbate distribution can compensate the charge locally, at times even producing measured contrast that is the opposite of the actual surface charge. This is discussed with respect to ferroelectric surfaces below, but is sometimes noted on electrically active grain boundaries.[147] A recent comparison of the surface potential of $SrTiO_3$ grain boundaries in air and in UHV demonstrated a sign reversal of grain boundary contrast.[148] This phenomena does not eliminate the usefulness of ambient measurements, but must be accounted for in qualitative and quantitative data interpretation.

(2) Polarization and Domain Dynamics in Ferroelectric Materials

Strong electromechanical coupling, high dielectric constants and the ability of materials to sustain spontaneous polarization below the Curie temperature make ferroelectrics one of the most fascinating materials and constitutes the basis for wide technological applicability.[149–151] Immediately after discovery of ferroelectricity in the perovskite $BaTiO_3$ and related perovskites simultaneously in the U.S.A., Russia and Japan in 1940s, these materials were recognized as promising materials for the submarine sonar arrays, heralding the onset of intensive research in the field. In more than half a century since then, numerous applications as sensors, actuators, transducers, electronic, and electrooptical materials have emerged. In the last decade, the development of deposition techniques for epitaxial ferroelectric thin films and advanced ceramic fabrication has resulted in numerous novel applications such as microelectromechanical systems (MEMS).[152–154] The ability of ferroelectric materials to exist in two or more polarized states, conserve polarization for a long period of time and change polarization in a field allows consideration for non-volatile computer memory devices (FeRAM).[155–157]

Generally, the properties of ferroelectric crystals, thin films, and ceramics, are averaged over ferroelectric domain structures. The domain structure significantly influences many physical properties, such as piezoelectricity, electrooptical properties, hysteresis, and switching behavior. High correlation energy (as compared to ferromagnetic materials) and multiple electromechanical coupling in ferroelectric compounds imply that the domain structure is strongly influenced by stress fields in the material. These effects are especially pronounced in epitaxial films, in which coupling to the substrate can stabilize specific domain structures and change thermodynamic parameters (e.g., T_c) of ferroelectric compound.[158–161] Complete description of the ferroelectric structure requires not only morphological information on domain structure but also on electrical and electromechanical interactions between domains including local stress and electric fields, as well as on dynamic domain behavior and structure property relationships within a single domain.

The formation and static properties of domains in bulk crystalline ferroelectrics have been extensively studied by polarizing optical microscopy, etching, surface decoration, etc.[162–164] However, these methods provide relatively low spatial resolution, of the order of 1 μm, limited by optical diffraction limit. In the last decade, the development of scanning near field optical microscopy[2] has allowed imaging of optical and electrooptical properties of ferroelectric materials with ~100 nm resolution.

Higher spatial resolution can be achieved by electron beam-based probes such as scanning and transmission electron microscopies. However, sample charging, local heating, and beam damage can cause problems. As a result, only a relatively small number of *in situ* experiments on domain wall motion under applied lateral bias or ferroelectric phase transition by optical microscopy,[165,166] scanning,[167,168] and transmission[169–175] electron microscopy have been reported.

In addition to surface topography, chemical reactivity, and optical properties, the electronic properties of ferroelectric surfaces and interfaces are also affected by the polarization charge, as exemplified by such phenomena as ferroelectric electron emission,[176,177] polarization-dependent work function,[178] polarization-dependent acid dissolution,[162] and metal photodeposition.[179,180,181] For example, for $BaTiO_3$, polarization charge is ~0.26 C/m^2 corresponding to $\frac{1}{4}$ of an electron per unit cell. This surface charge is sufficient to induce accumulation or strong inversion, affecting the photoelectric and catalytic activity of the surface. A detailed discussion of surface space charge phenomena in ferroelectric semiconductors is given by Fridkin.[182] Domain structure (and hence the polarization charge distribution) can be controlled and, in fact, engineered. It was shown by Ahn.[183,184] that a ferroelectric field effect in ferroelectric/semiconductor heterostructures could result in a metal/insulator

transition dependent on the local polarization orientation, introducing new paradigms in oxide electronics. However, applications such as ferroelectric recording, thin film research, and heterostructures require the ability to image domain structures and probe the materials properties, including surface charge density, local electromechanical activity, elasticity, electrooptical coefficients, inside a single domain on the nanometer scale.

A breakthrough in ferroelectric imaging was achieved after the invention of SPM-based techniques. Contact and intermittent mode atomic force microscopy, along with lateral force microscopy, has been widely used to characterize domain-related topographic features.[185–193] Electrostatic scanning probe techniques such as electrostatic force microscopy (EFM) and SSPM have been used to image electric fields associated with polarization charge on ferroelectric surfaces.[194–198] Motivated by the concept of high-density ferroelectric memory, many groups used a conductive tip to induce local domain orientation and imaged the result with PFM. It was quickly realized that different SPM techniques are sensitive to different polarization-related phenomena, providing complementary information on local properties.[199] In most cases, SPM provides contrast that changes abruptly at the domain walls, providing readily observable domain images. However, while domains can be easily visualized in the SPM image, quantitative and even qualitative correlation of SPM data with polarization orientation is often non-trivial.

As an example, SSPM imaging of electrostatic fields above the ferroelectric surfaces is illustrated below. Figure 15(a) shows surface topography and surface potential images of a (100) surface of ferroelectric $BaTiO_3$. Surface topography exhibits characteristic corrugations at the positions of 90° domain walls between in-plane *a* and out-of-plane *c* domains. The corrugation angle is $\theta = \pi/2 - \arctan(a/c)$, where *a* and *c* are unit cell parameters of the tetragonal unit cell. Formation of 180° domain walls does not influence the surface topography, but affects the surface polarization, since polarization charge density, σ, is directly determined by the out-of-plane component of the polarization vector, $\sigma = \mathbf{P} \cdot \mathbf{n}$, where $\mathbf{n}$ is surface normal. The surface potential image in Fig. 16(b) illustrates that domains in flat regions have distinct bright and dark contrasts, whereas in other regions potential contrast is uniform. The latter can unambiguously be attributed to in-plane *a* domains, whereas the former corresponds to out-of-plane *c* domains of opposite polarities. The domain image in Fig. 15 can thus be interpreted by alternating *a* and *c* domains with 90° domain boundaries in the *y* direction and 180° domain walls along the *x* direction. However, SSPM does not unambiguously distinguish c^+ and c^- domains. Indeed, for the ideal ferroelectric surface, surface charge is positive for polarization vector oriented upward and negative for polarization vector oriented downward, suggesting that bright domains should be identified as c^+ and dark as c^-. Detailed analysis of SSPM image mechanism suggests that the potential contrast is due to the dipole layer formed by polarization charge and equal to magnitude screening charge.[37] Screening can be either due to surface adsorbates (extrinsic) or charge carriers in the material (intrinsic). Such analyses can establish the dipole moment of the double layer; however, the unambiguous relationship between the SSPM contrast and domain orientation cannot be obtained.

This goal can be achieved only by observation of dynamic domain behavior under varying conditions, e.g., temperature, or during domain wall motion. Such studies allow dynamic behavior, e.g., domain wall velocity and nucleation and growth of domains, to be visualized. At the same time, the change of SPM contrast provides insight into SPM imaging mechanism. Figures 15(c) and (d) show the domain contrast above the ferroelectric Curie temperature. Note that surface corrugations disappeared, indicative of the transition to cubic phase, while surface potential features remained with a temporarily increased magnitude. These features disappear with time of the order of several hours, as illustrated in Figs. 15(e) and (f). This behavior, as well as more complex phenomena of temperature-induced potential inversion,[40] is due to screening of polarization by adsorbing charges and slow relaxation following the initial rapid response of polarization to temperature. It has also been shown that in most cases the sign of the surface charge is that of the compensating species, i.e., opposite that of the domain polarization charge.

Similar ambiguities have arisen in the PFM observations of the phase transition. Luo *et al.*[200] found that the temperature dependence of PFM contrast of triglycine sulphate (TGS) near the Curie temperature was similar to that of the spontaneous polarization rather than the piezoelectric coefficient. The gradual change in potential was attributed to the dominance of electrostatic interactions due to the charged surface,[201] since the electromechanical response based on the piezoelectric coefficient would diverge in the vicinity of the Curie temperature. Contradictory behavior was observed in the existence of a lateral PFM signal, which could not result from surface charge alone,[91,202] the absence of relaxation behavior that is characteristic of compensation charge,[37,203] as well as numerous observations using both EFM/SSPM and PFM[204,205] that clearly pointed to a significant electromechanical contribution to PFM contrast. The discrepancies can be resolved with reference to Fig. 4. Experiments done under conditions in which the sample/tip interaction was influenced by electrostatic forces as well as piezoelectric de-

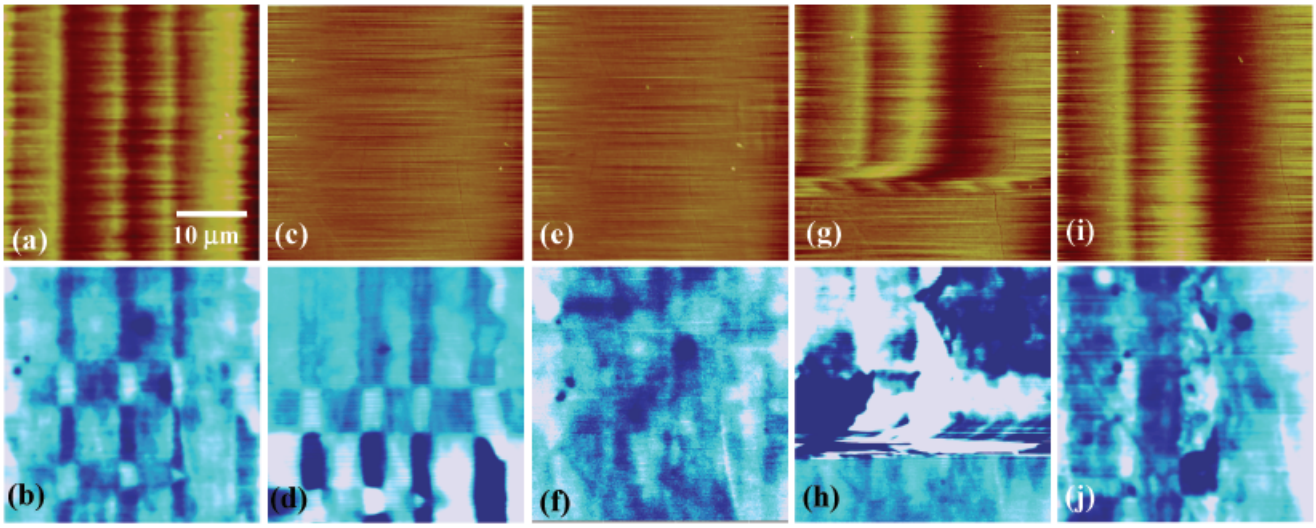

Fig. 15. Surface topography and potential distribution at $BaTiO_3$ (100) surface before ferroelectric phase transition at 125°C (a,b), 4 min after transition (c,d), and after 2.5 h annealing at 140°C (e,f), during the reverse transition (g,h) and 1 h after the transition (i,j). Images are acquired from bottom to top. Scale is 30 nm (a,c,e), 0.05 V (b), 0.1 V (d,f), 0.5 V (g), and 0.05 V (i). Reprinted with permission from *J. Appl. Phys.*, **87,** 3950 (2000).

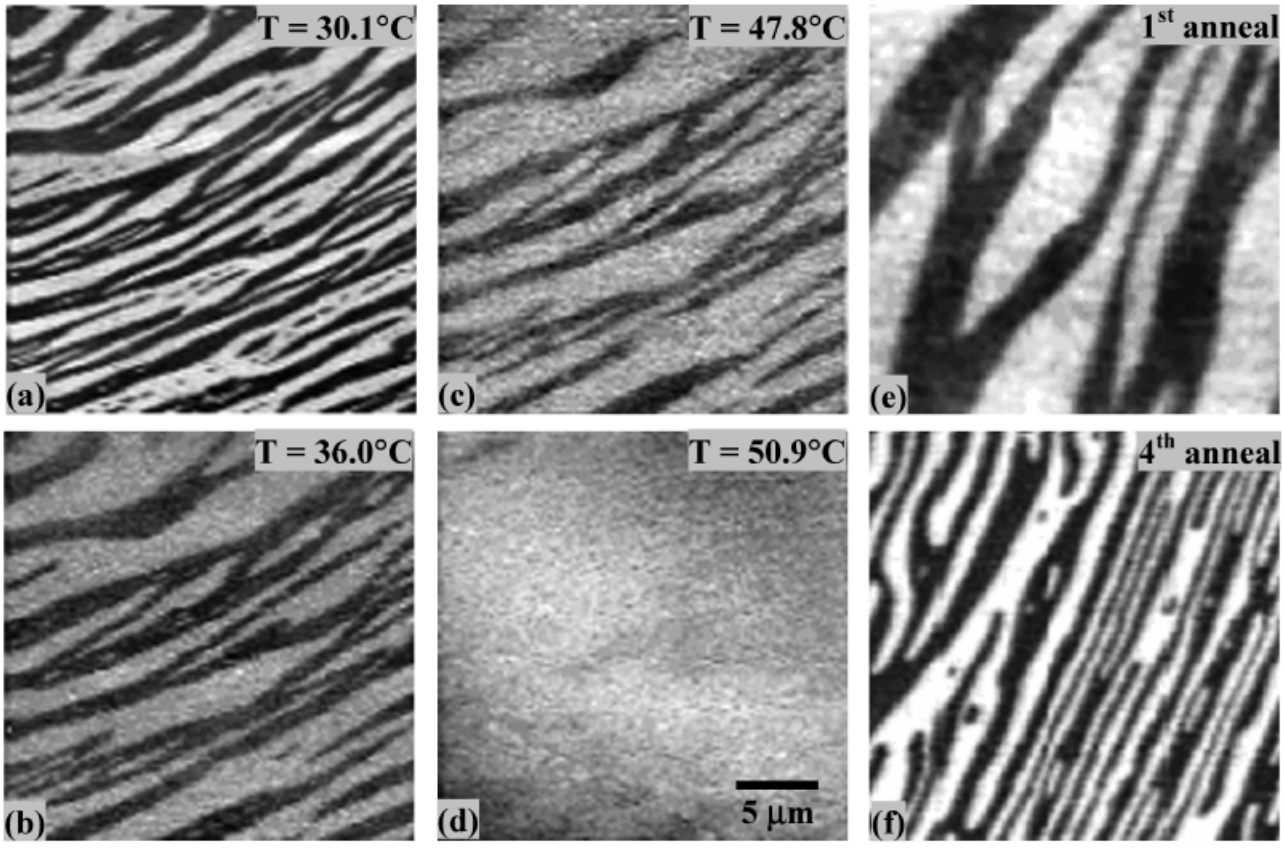

Fig. 16. Temperature dynamics of the domain structure of triglycinsylphate (TGS) surface. Images are acquired at (a) 30.1°C, (b) 46.0°C, (c) 47.8°C, and (d) 50.9°C. Partially reprinted with permission from *Appl. Phys. Lett*., **76,** 1321–3 (2000)]. Piezoresponse images (e) after one annealing cycle above T_c and (f) after four annealing cycles. Reprinted with permission from *Phys. Rev. B*, **66,** 024104 (2002).

formation obtained different results than those with conditions squarely in the SI regime, where the signal is directly related to the piezoelectric coefficient.

Figure 16 shows the thermal evolution of the domain structure in TGS probed by variable temperature PFM.[203,206,207] A gradual decrease in domain contrast with temperature and almost complete disappearance of contrast above T_c are observed, as illustrated in Figs. 16(a)–(d). This behavior is expected for the contact limited strong indentation, when the dielectric gap effect between the tip and the surface dominates the imaging and mitigates the effect of increase in d_{33} close to phase transition. Note that cycling through ferroelectric phase transition results in an emergence of a new domain structure (Figs. 16(e) and (f)).

The unique feature of PFM compared to non-contact electrostatic SPMs is the extremely high resolution that allows imaging ferroelectric phenomena on the sub-10 nm level.

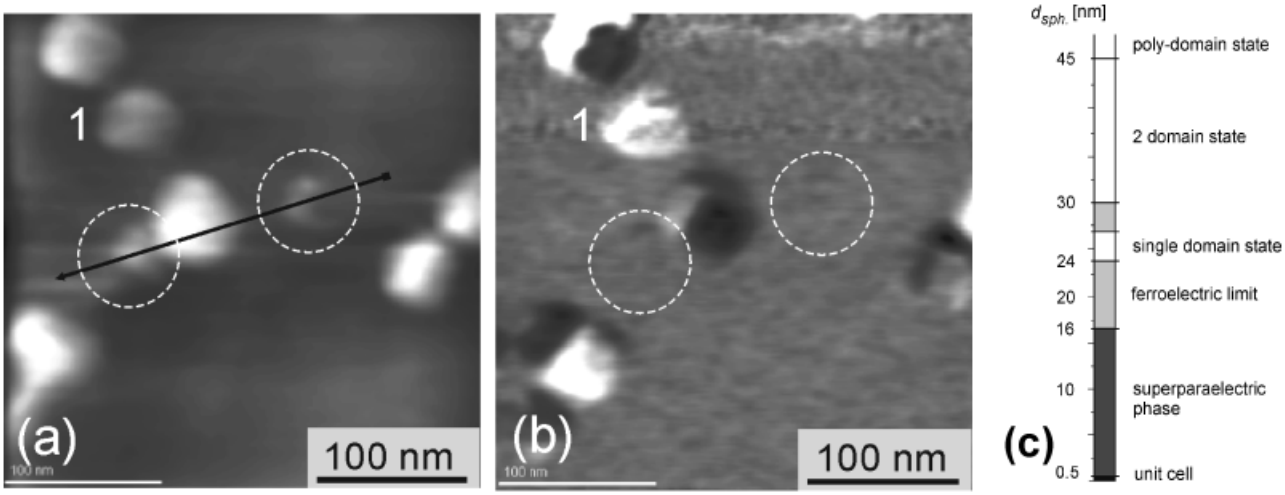

Fig. 17. Surface topography (a) of $PbTiO_3$ sample illustrating nine PTO grains of sizes between 100 nm down to 18 nm. In the PFM image (b) the grains of the size of 18 nm (indicated by the circles) are not visible, leading to the assumption that they do not have any electromechanical activity. Note, all ferroelectric grains exhibit two domains except one (denoted with 1), which is mono-domain and has a volume of about 7200 nm^3. (c) Size-dependent domain configuration of separated PTO grains as a function of the corresponding spherical particle diameter. The ferroelectric limit for PTO is between 16.5 and 24 nm. Grains which are smaller than 16.5 nm are in the superparaelectric phase. Reprinted with permission from *Nanotechnology*, **14,** 250 (2003).

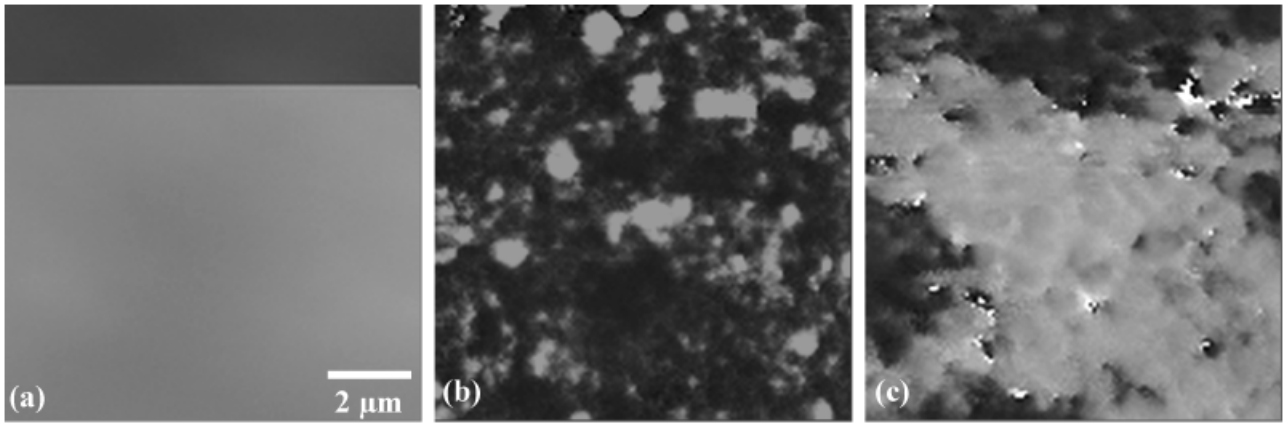

Fig. 18. Domain images as a function of fatigue cycles; (a) 10^2, (b) 10^5, and (c) 10^7 cycles. The upper dark part of (a) was obtained by applying the opposite field. Reprinted with permission from *Appl. Phys. Lett.*, **72,** 2763 (2002).

Depending on the indentation conditions, lateral resolution in PFM is limited either by tip radius of curvature (10–50 nm) in a weak indentation regime or tip–surface contact area (3–10 nm) in a strong indentation regime. This sensitivity to extremely localized electromechanical response paves the way to study phenomena such as ferroelectric size effects and size dependence in ferroelectric responses. It has long been realized that collective phenomena such as ferroelectricity or ferromagnetism can exist only in a finite volume of material. However, the critical size below which ferroelectric ordering becomes unstable and size affects materials properties remains a matter of extensive debate.

Generally, the reduction in grain size for ferroelectric ceramics or film thickness for thin film results in a change of domain structure, increase in coercive field, decrease in piezoelectric constant, lowering of transition temperature, and decrease in remanent polarization. In many cases, the intrinsic ferroelectric size effect cannot be distinguished from the effects associated with the formation of non-ferroelectric layers on the surfaces and interfaces, which become progressively dominant for small sample sizes. Recently, an approach to study local size effect has been demonstrated by combining the microfabricated ferroelectric capacitors of given size with PFM response and hysteresis loop measurements.[208] It was shown that reduction in lateral capacitor size from 1000 to 200 nm results in an increase in electromechanical activity. This behavior was ascribed to the reduction of clamping and the fraction of 90° domain walls for smaller capacitors. An extensive study of size effects in ferroelectrics was performed by Roelofs.[99] $PbTiO_3$ nanoparticles with different sizes were fabricated with a sol–gel method utilizing precursor solution with different concentrations. The particle size can be determined from topographic AFM image, while electromechanical activity and hence ferroelectric properties can be determined from PFM image, as illustrated in Fig. 17. It was found that relatively large particles exist in multidomain state and several polarization orientations can be detected within a single isolated grain. On decreasing the size of the individual PTO grains to ~50 nm, the domain structure considerably simplifies and can vary from laminar to two domain state. Below ~25 nm particles exist predominantly in a single domain state. As illustrated in Fig. 17, particles smaller than ~20 nm, while visible on the topographic image, cannot be detected on vertical or lateral PFM image, suggesting that they exist in the superparaelectric phase. Thus, obtained size dependence of ferroelectric properties is summarized in Fig. 17(c).

Another problem that has attracted significant attention is ferroelectric fatigue, i.e., loss of switchable polarization with switching cycles. This is a particularly important parameter for applications such as non-volatile ferroelectric memories (FeRAMs). One of the primary explanations for fatigue is domain wall pinning by oxygen vacancies and interface defects. Colla *et al.*[209] and Hong[210] have studied the polarization dynamics in ferroelectric thin films as a function of number of switching cycles. Shown in Figs. 18(a)–(c) are PFM phase images of PZT thin films on PT substrates after 10^1, 10^5, and 10^7 switching cycles. After a small number of switching cycles, polarization can be easily switched and the resulting uniform potential distribution is imaged by the PFM tip, as illustrated in Fig. 18(a). Polarization is switched during the imaging, as indicated by the change of phase contrast from positive to negative in the middle of the scan. Figure 18(b) shows the PFM phase image after 10^5 cycles (corresponding to ~30% reduction in switchable polarization) after the application of about 15 V to the bottom electrode (BE). For a pristine surface, this will result in a uniform dark contrast in the image; however, in the fatigued state both dark regions and bright islands with frozen polarization can be seen. The degree of fatigue characterized by the bright area is about 21%, which fits well with the macroscopic ferroelectric measurements. Figure 18(c) illustrates switching behavior after 10^7 cycles. The bright regions are the frozen domains and the calculated degree of fatigue is 70%. By poling in the opposite direction, the phase becomes homogeneous. These results clearly show that the fatigue in Pt–PZT–Pt ferroelectric capacitors takes place region by region and that the orientation of the frozen polarization can have a preferential direction from the top to the bottom electrode.

III. Conclusions: Future View

The future will undoubtedly see the continued expansion of functionality of SPM-based characterization tools. The development of multiple modulation approaches and the use of higher-order harmonic signals have allowed complex properties to be quantified with high spatial resolution. While these trends have been outlined here for electrostatic and transport-related probes, they also occurr with magnetic and optically based probes. Future developments will certainly involve two strategies: a move toward combining electronic/magnetic/optical probes for more complete characterization and the drive to achieve atomic resolution of force-detected properties.

The two case studies presented here, while not comprehensive reviews of those fields, provide a flavor of the insight SPM can bring to classic materials science issues. Other materials based fields in which SPM plays an increasing role are nanoparticles in general, optical quantum dots, nanowires, composites, block copolymers, quantum devices (single electron transistors, etc.). In particular, any time spatial inhomogeneity of properties occurs on the submicron to nanometer length scale, SPM will provide unique insight and is sometimes the only approach to intractable problems.

References

[1]G. S. Rohrer, V. Henrich, and D. A. Bonnell, "Structure of the Reduced TiO_2 (110) Surface Determined by STM," *Science (Washington, D.C.)*, **250**, 1230–41 (1991).

[2]D. A. Bonnell, "Scanning Tunneling Microscopy and Spectroscopy of Oxide Surfaces," *Progr. Surf. Sci.*, **57**, 187–252 (1998).

[3]T. Sano, D. M. Saylor, and G. S. Rohrer, "Surface Energy Anisotropy of $SrTio_3$ at 1400°C in Air," *J. Am. Ceram. Soc.*, **86**, 1933–9 (2003).

[4]V. R. Vedula, S. J. Glass, D. M. Saylor, G. S. Rohrer, W. C. Carter, and S. A. Langer, "Residual Stress Predictions in Polycrystalline Alumina," *J. Am. Ceram. Soc.*, **84**, 2947–54 (2001).

[5]D. A. Bonnell and J. Kiely, "Local Plasticity at Metal Ceramic Interfaces," *Phys. Stat. Sol. A*, **166**, 7–17 (1998).

[6]R. L. Smith and G. S. Rohrer, "An Atomic Force Microscopy Study of the Morphological Evolution of the MoO_3(010) Surface During Reduction Reactions," *J. Catalysis*, **163**, 12–7 (1996).

[7]R. L. Smith and G. S. Rohrer, "The Morphological Evolution of the MoO_3(010) Surface During the Partial Oxidation of Methanol," *J. Catalysis*, **180**, 270–8 (1998).

[8]As Determined from COMPENDEX for 2002.

[9]D. A. Bonnell (ed.), *Scanning Probe Microscopy and Spectroscopy: Theory, Techniques and Applications*, 2nd edition, VCH, New York, 2000.

[10]R. Wiesendanger (ed.), *Scanning Probe Microscopy and Spectroscopy-Methods and Applications*. Cambridge University Press, Cambridge, UK, 1994.

[11]G. Friedbacher and H. Fuchs, "Classification of Scanning Probe Microscopies—(Technical Report)," *Pure Appl. Chem.*, **71**, 1337–57 (1999).

[12]L. Bottomley, "Scanning Probe Microscopy," *Anal. Chem.*, **70**, 425R–75R (1998) and the References Therein.

[13]W. Hofer, A. Foster, and A. Shluger, "Theories of Scanning Probe Microscopes at the Atomic Scale," *Rev. Mod. Phys.*, **75**, 1287–331 (2003).

[14]R. Garcia and R. Perez, "Dynamic Atomic Force Microscopy Methods," *Surf. Sci. Rep.*, **47**, 197–301 (2002).

[15]G. Binnig, C. F. Quate, and Ch. Gerber, "Atomic Force Microscope," *Phys. Rev. Lett.*, **56**, 930 (1986).

[16]C. Argento and R. H. French, "Parametric Tip Model and Force–Distance Relation for Hamaker Constant Determination from Atomic Force Microscopy," *J. Appl. Phys.*, **80**, 6081–90 (1996).

[17]R. Bennewitz, A. S. Foster, L. N. Kantorovich, M. Bammerlin, Ch. Loppacher, S. Schar, M. Guggisberg, E. Meyer, and A. L. Shluger, "Atomically Resolved Edges and Kinks of NaCl Islands on Cu(111): Experiment and Theory," *Phys. Rev. B*, **62**, 2074–84 (2000).

[18]A. S. Foster, A. L. Shluger, and R. M. Nieminem, "Realistic Model Tips in Simulations of nc-AFM," *Nanotechnology*, **15**, S60–4 (2004).

[19]B. Capella and G. Dietler, "Force-Distance Curves by Atomic Force Microscopy," *Surf. Sci. Rep.*, **34**, 1–104 (1999).

[20]T. R. Albrecht, P. Grütter, and D. Rugar, "Frequency Modulation Detection Using High-Q Cantilevers for Enhanced Force Microscope Sensitivity," *J. Appl. Phys.*, **69**, 668–73 (1991).

[21]In many cases, contact mode AFM provides "lattice imaging" when the periodicity of sample surface is clearly seen, but the contact between the tip and the surface occurs at multiple regions, precluding true atomic resolution when individual atomic defects can be observed.

[22]F. J. Giessibl, "Atomic Resolution of the Silicon (111)-(7 × 7) Surface by Atomic Force Microscopy," *Science*, **267**, 68–71 (1995).

[23]Y. Sugawara, M. Ohta, H. Ueyama, and S. Morita, "Defect Motion on an InP(110) Surface Observed with Noncontact Atomic Force Microscopy," *Science*, **270**, 1646–8 (1995).

[24]S. Kitamura and M. Iwatsuki, "Observation of 7 × 7 Reconstructed Structure on the Silicon (111) Surface Using Ultrahigh Vacuum Noncontact Atomic Force Microscopy," *Jpn. J. Appl. Phys.*, **35**, L145–8 (1995).

[25]T. Kubo and H. Nozoye, "Surface Structure of $SrTiO_3$(100)-(sqrt[5] × sqrt[5])-R26.6°," *Phys. Rev. Lett.*, **86**, 1801–4 (2001).

[26]S. Orisaka, T. Minobe, T. Uchihashi, V. Sugawara, and S. Morita, "The Atomic Resolution Imaging of Metallic Ag(111) Surface by Noncontact Atomic Force Microscope," *Appl. Surf. Sci.*, **140**, 243–6 (1999).

[27]C. Loppacher, M. Bammerlin, M. Guggisberg, S. Schar, A. Baratoff, E. Meyer, and H. J. Güntherodt, "Dynamic Force Microscopy of Copper Surfaces: Atomic Resolution and Distance Dependence of Tip–Sample Interaction and Tunneling Current," *Phys. Rev. B*, **62**, 16944–9 (2000).

[28]C. Loppacher, M. Bammerlin, M. Guggisberg, F. Barttison, R. Bennewitz, S. Rast, A. Baratoff, E. Meyer, and H. J. Güntherodt, "Phase Variation Experiments in Non-Contact Dynamic Force Microscopy Using Phase Locked Loop Techniques," *Appl. Surf. Sci.*, **140**, 287–92 (1999).

[29]T. Minobe, T. Uchihashi, T. Tsukamoto, S. Orisaka, V. Sugawara, and S. Morita, "Distance Dependence of Noncontact-AFM Image Contrast on Si(111) × Ag Structure," *Appl. Surf. Sci.*, **140**, 298–303 (1999).

[30]M. A. Lantz, H. J. Hug, P. J. A. van Schendel, R. Hoffmann, S. Martin, A. Baratoff, A. Abdurixit, and H.-J. Güntherodt, "Low Temperature Scanning Force Microscopy of the Si(111)-(7 × 7) Surface," *Phys. Rev. Lett.*, **84**, 2642–5 (2000).

[31]W. Allers, A. Schwarz, U. Schwarz, and R. Wiesendanger, "Dynamic Scanning Force Microscopy at Low Temperatures on a Noble-Gas Crystal: Atomic Resolution on the Xenon(111) Surface," *Europhys. Lett.*, **48**, 276–9 (1999).

[32]J. M. R. Weaver and D. W. Abraham, "High Resolution Atomic Force Microscopy Potentiometry," *J. Vac. Sci. Technol.*, **B9**, 1559–61 (1991).

[33]M. Nonnenmacher, M. P. O'Boyle, and H. K. Wickramasinghe, "Kelvin Probe Force Microscopy," *Appl. Phys. Lett.*, **58**, 2921–3 (1991).

[34]A. K. Henning and T. Hochwitz, "Scanning Probe Microscopy for 2-D Semiconductor Dopant Profiling and Device Failure Analysis," *Mater. Sci. Eng.*, **B 42**, 88–98 (1996).

[35]H. O. Jacobs, P. Leuchtmann, O. J. Homan, and A. Stemmer, "Resolution and Contrast in Kelvin Probe Force Microscopy," *J. Appl. Phys.*, **84**, 1168–73 (1998).

[36]A. Efimov and S R. Cohen, "Simulation and Correction of Geometric Distortions in Scanning Kelvin Probe Microscopy," *J. Vac. Sci. Technol. A*, **18**, 1051–5 (2000).

[37]S. V. Kalinin and D. A. Bonnell, "Local Potential and Polarization Screening on Ferroelectric Surfaces," *Phys. Rev. B*, **63**, 125411 (2001).

[38]S. Cunningham, I. A. Larkin, and J. H. Davis, "Noncontact Scanning Probe Microscope Potentiometry of Surface Charge Patches: Origin and Interpretation of Time-Dependent Signals," *Appl. Phys. Lett.*, **73**, 123–5 (1998).

[39]K. Franke, H. Huelz, and M. Weihnacht, "How to Extract Spontaneous Polarization Information from Experimental Data in Electric Force Microscopy," *Surf. Sci.*, **415**, 178–82 (1998).

[40]S. V. Kalinin, C. Y. Johnson, and D. A. Bonnell, "Domain Polarity and Temperature Induced Potential Inversion on the $BaTiO_3$(100) Surface," *J. Appl. Phys.*, **91**, 3816–23 (2002).

[41]C. Donolato, "Electrostatic Tip-Sample Interaction in Immersion Force Microscopy of Semiconductors," *Phys. Rev. B*, **54**, 1478–81 (1996).

[42]Y. Leng, C. C. Williams, L. C. Su, and G. B. Stringfellow, "Atomic Ordering of GaInP Studied by Kelvin Probe Force Microscopy," *Appl. Phys. Lett.*, **66**, 1264–6 (1995).

[43]M. Tanimoto and O. Vatel, "Kelvin Probe Force Microscopy for Characterization of Semiconductor Devices and Processes," *J. Vac. Sci. Technol.*, **B 14**, 1547–51 (1996).

[44]T. Hochwitz, A. K. Henning, C. Levey, C. Daghlian, J. Slinkman, J. Never, P. Kaszuba, R. Gluck, R. Wells, J. Pekarik, and R. Finch, "Imaging Integrated Circuit Dopant Profiles with the Force-Based Scanning Kelvin Probe Microscope," *J. Vac. Sci. Technol.*, **B 14**, 440–6 (1996).

[45]M. Fujihira, "Kelvin Probe Force Microscopy of Molecular Surfaces," *Annu. Rev. Mater. Sci.*, **12**, 353–80 (1999).

[46]X. Q. Chen, H. Yamada, T. Horiuchi, K. Matsushige, S. Watanabe, M. Kawai, and P. S. Weiss, "Surface Potential of Ferroelectric Thin Films Investigated by Scanning Probe Microscopy," *J. Vac. Sci. Technol.*, **B 17**, 1930–4 (1999).

[47]T. Tybell, C. H. Ahn, and J.-M. Triscone, "Ferroelectricity in Thin Perovskite Films," *Appl. Phys. Lett.*, **75**, 856–8 (1999).

[48]P. M. Bridger, Z. Z. Bandic, E. C. Piquette, and T. C. McGill, "Measurement of Induced Surface Charges, Contact Potentials, and Surface States in GaN by Electric Force Microscopy," *Appl. Phys. Lett.*, **74**, 3522–4 (1999).

[49]Q. Xu and J. W. P. Hsu, "Electrostatic Force Microscopy Studies of Surface Defects on GaAs/Ge Films," *J. Appl. Phys.*, **85**, 2465–72 (1999).

[50]A. Chavez-Pirson, O. Vatel, M. Tanimoto, H. Ando, H. Iwamura, and H. Kanbe, "Nanometer-Scale Imaging of Potential Profiles in Optically Excited n–i–p–i Heterostructure Using Kelvin Probe Force Microscopy," *Appl. Phys. Lett.*, **67**, 3069–71 (1995).

[51]T. Meoded, R. Shikler, N. Fried, and Y. Rosenwaks, "Direct Measurement of Minority Carriers Diffusion Length Using Kelvin Probe Force Microscopy," *Appl. Phys. Lett.*, **75**, 2435–7 (1999).

[52]S. V. Kalinin and D. A. Bonnell, "Dynamic Behavior of Domain-Related Topography and Surface Potential on the $BaTiO_3$ (100) Surface by Variable Temperature Scanning Surface Potential Microscopy," *Z. Metallkd.*, **90**, 983–9 (1999).

[53]B. D. Huey, D. Lisjak, and D. A. Bonnell, "Nanometer-Scale Variations in Interface Potential by Scanning Probe Microscopy," *J. Am. Ceram. Soc.*, **82** [7] 1941–4 (1999).

[54]S. V. Kalinin and D. A. Bonnell, "Local Potential at Atomically Abrupt Oxide Grain Boundaries by Scanning Probe Microscopy;" *Solid State Phen.*, **80–81**, 33–44 (2001).

[55]V. Meunier, Private Communications.

[56]P. De Wolf, R. Stephenson, T. Trenkler, T. Clarysse, T. Hantschel, and W. Vandervorst, "Status and Review of Two-Dimensional Carrier and Dopant Profiling Using Scanning Probe Microscopy," *J. Vac. Sci. Technol.*, **B 18**, 361–8 (2000).

[57]P. De Wolf, J. Snauwaert, L. Hellemans, T. Clarysse, W. Vandervorst, M. D'Olieslaeger, and D. Quaeyhaegens, "Lateral and Vertical Dopant Profiling in Semiconductors by Atomic Force Microscopy Using Conducting Tips," *J. Vac. Sci. Technol.*, **A 13**, 1699–704 (1995).

[58]P. De Wolf, T. Clarysse, and W. Vandervorst, "Low Weight Spreading Resistance Profiling of Ultrashallow Dopant Profiles," *J. Vac. Sci. Technol.*, **B 16**, 401–5 (1998).

[59]J. R. Matey and J. Blanc, "Scanning Capacitance Microscopy," *J. Appl. Phys.*, **57**, 1437–44 (1985).

[60]R. C. Barrett and C. F. Quate, "Charge Storage in a Nitride–Oxide–Silicon Medium by Scanning Capacitance Microscopy," *J. Appl. Phys.*, **70**, 2725–33 (1991).

[61]Y. Huang, C. C. Williams, and M. A. Wendman, "Quantitative Two-Dimensional Dopant Profiling of Abrupt Dopant Profiles by Cross-Sectional Scanning Capacitance Microscopy," *J. Vac. Sci. Technol.*, **A 14**, 1168–71 (1996).

[62]T. Hantschel, P. Niedermann, T. Trenkler, and W. Vandervorst, "Highly Conductive Diamond Probes for Scanning Spreading Resistance Microscopy," *Appl. Phys. Lett.*, **76**, 1603–5 (2000).

[63]J. T. Marchiando and J. J. Kopanski, "Regression Procedure for Determining the Dopant Profile in Semiconductors from Scanning Capacitance Microscopy Data," *J. Appl. Phys.*, **92**, 5798–809 (2002).

[64]J. Yang and F. C. J. Kong, "Simulation of Interface States Effect on the Scanning Capacitance Microscopy Measurement of p–n Junctions," *Appl. Phys. Lett.*, **81**, 4973–5 (2002).

[65]S. Lányi, J. Török, and P. Rehurek, "Imaging Conducting Surfaces and Dielectric Films by a Scanning Capacitance Microscope," *J. Vac. Sci. Technol.*, **B 14**, 892–6 (1996).

[66]S. Belaidi, P. Girard, and G. Leveque, "Electrostatic Forces Acting on the Tip in Atomic Force Microscopy: Modelization and Comparison with Analytic Expressions," *J. Appl. Phys.*, **81**, 1023–30 (1997).
[67]J. R. Macdonald (ed.), *Impedance Spectroscopy: Emphasizing Solid Materials and Systems*. Wiley, New York, 1987.
[68]S. V. Kalinin and D. A. Bonnell, "Scanning Impedance Microscopy of Electroactive Interfaces," *Appl. Phys. Lett.*, **78**, 1306–8 (2001).
[69]S. V. Kalinin, M. R. Suchomel, P. K. Davies, and D. A. Bonnell, "Potential and Impedance Imaging of Polycrystalline $BiFeO_3$ Ceramics," *J. Am. Cer. Soc.*, **85**, 3011–7 (2003).
[70]M. A. Eriksson, R. G. Beck, M. Topinka, J. A. Katine, R. M. Westervelt, K. L. Campman, and A. C. Gossard, "Cryogenic Scanning Probe Characterization of Semiconductor Nanostructures," *Appl. Phys. Lett.*, **69**, 671–3 (1996).
[71]S. J. Tans and C. Dekker, "Molecular Transistors: Potential Modulations Along Carbon Nanotubes," *Nature*, **404**, 834–5 (2000).
[72]S. V. Kalinin, D. A. Bonnell, M. Freitag, and A. T. Johnson, "Tip-Gating Effect in Scanning Impedance Microscopy of Nanoelectronic Devices," *Appl. Phys. Lett.*, **81**, 5219–21 (2002).
[73]S. V. Kalinin and D. A. Bonnell, "Scanning Impedance Microscopy of an Active Schottky Barrier Diode," *J. Appl. Phys.*, **95**, 832–9 (2002).
[74]R. Shao, S. V. Kalinin, and D. A. Bonnell, "Local Impedance Imaging and Spectroscopy of Polycrystalline ZnO Using Contact Atomic Force Microscopy," *Appl. Phys. Lett.*, **82**, 1869–71 (2003).
[75]R. O'Hayre, M. H. Lee, and F. B. Prinz, "Ionic and Electronic Impedance Imaging Using Atomic Force Microscopy," *J. Appl. Phys.*, **95**, 8382–92 (2004).
[76]R. O'Hayre, G. Feng, W. D. Nix, and F. B. Prinz, "Quantitative Impedance Measurement Using Atomic Force Microscopy," *J. Appl. Phys.*, **96**, 3540–9 (2004).
[77]A. Gruverman, "Ferroelectric Nanodomains;" pp. 359–75 in *Encyclopedia of Nanoscience and Nanotechnology*, Vol. 3. Edited by H. S. Nalwa. American Scientific Publishers, Los Angeles, 2004.
[78]C. Durkan and M. E. Welland, "Investigations into Local Ferroelectric Properties by Atomic Force Microscopy," *Ultramicroscopy*, **82**, 141–8 (2000).
[79]A. Gruverman, O. Kolosov, J. Hatano, K. Takahashi, and H. Tokumoto, "Domain Structure and Polarization Reversal in Ferroelectrics Studied by Atomic Force Microscopy," *J. Vac. Sci. Technol.*, **B 13**, 1095–9 (1995).
[80]K. Franke, H. Huelz, and M. Weihnacht, "How to Extract Spontaneous Polarization Information from Experimental Data in Electric Force Microscopy," *Surf. Sci.*, **415**, 178–82 (1998).
[81]S. Hong, J. Woo, H. Shin, J. U. Jeon, Y. E. Park, E. L. Colla, N. Setter, E. Kim, and K. No, "Principle of Ferroelectric Domain Imaging Using Atomic Force Microscope," *J. Appl. Phys.*, **89**, 1377–86 (2001).
[82]S. V. Kalinin and D. A. Bonnell, "Imaging Mechanism of Piezoresponse Force Microscopy of Ferroelectric Surfaces," *Phys. Rev. B*, **65**, 125408 (2002).
[83]C. Harnagea, "Local Piezoelectric Response and Domain Structures in Ferroelectric Thin Films Investigated by Voltage Modulated Force Microscopy," Dr. Rer. Nat. Thesis, Martin-Luther-Universität Halle Wittenberg, Halle, 2001, pp. 1–97.
[84]C. Ganpule, "Nanoscale Phenomena in Ferroelectric Thin Films," Ph.D. Thesis, University of Maryland, College Park, 2001.
[85]M. Abplanalp, "Piezoresponse Scanning Force Microscopy of Ferroelectric Domains," Ph.D. Thesis, Swiss Federal Institute of Technology, Zurich, 2001.
[86]S. V. Kalinin, "Nanoscale Phenomena at Oxide Surfaces and Interfaces by Scanning Probe Microscopy," Ph.D. Thesis, University of Pennsylvania, Philadelphia, 2002.
[87]S. V. Kalinin and D. A. Bonnell, "Contrast Mechanism Maps for Piezoresponse Force Microscopy," *J. Mater. Res.*, **17** [5] 936–9 (2002).
[88]S. V. Kalinin, E. Karapetian, and M. Kachanov, "Nanoelectromechanics of Piezoresponse Force Microscopy," *Phys. Rev. B*, **70**, 184101 (2004).
[89]L. M. Eng, H. J. Güntherodt, G. A. Schneider, U. Kopke, and J. Munoz Saldana, "Nanoscale Reconstruction of Surface Crystallography from Three-Dimensional Polarization Distribution in Ferroelectric Barium–Titanate Ceramics," *Appl. Phys. Lett.*, **74**, 233–5 (1999).
[90]A. Roelofs, U. Boettger, R. Waser, F. Schlaphof, S. Trogisch, and L. M. Eng, "Differentiating 180° and 90° Switching of Ferroelectric Domains with Three-Dimensional Piezoresponse Force Microscopy," *Appl. Phys. Lett.*, **77**, 3444–6 (2000).
[91]C. Harnagea, A. Pignolet, M. Alexe, and D. Hesse, "Piezoresponse Scanning Force Microscopy: What Quantitative Information Can We Really Get Out of the Piezoresponse Measurements on Ferroelectric Thin Films," *Integr. Ferroelectr.*, **38**, 23–9 (2001).
[92]B. J. Rodriguez, A. Gruverman, A. I. Kingon, R. J. Nemanich, and J. S. Cross, "Three-Dimensional High-Resolution Reconstruction of Polarization in Ferroelectric Capacitors by Piezoresponse Force Microscopy," *J. Appl. Phys.*, **95** [4] 1958–62 (2004).
[93]S. V. Kalinin, B. J. Rodriguez, S. Jesse, J. Shin, A. P. Baddorf, P. Gupta, H. Jain, D. B. Williams, and A. Gruverman, "Vector Piezoresponse Force Microscopy," to be published.
[94]S. V. Kalinin, B. J. Rodriguez, S. Jesse, A. Gruverman, "Orientational Imaging by Electromechanical Scanning Probe Microscopy," to be Submitted.
[95]V. Likodimos, M. Labardi, and M. Allegrini, "Kinetics of Ferroelectric Domains Investigated by Scanning Force Microscopy," *Phys. Rev. B*, **61**, 14440–7 (2000).
[96]C. Harnagea, M. Alexe, D. Hesse, and A. Pignolet, "Contact Resonances in Voltage-Modulated Force Microscopy," *Appl. Phys. Lett.*, **83** (2) 338–40 (2003).
[97]X. M. Lu, F. Schlaphof, S. Grafstroem, C. Loppacher, L. M. Eng, G. Suchaneck, and G. Gerlach, "Scanning Force Microscopy Investigation of the $Pb(Zr_{0.25}Ti_{0.75})O_3$/Pt Interface," *Appl. Phys. Lett.*, **81**, 3215–7 (2002).
[98]A. Roelofs, T. Schneller, K. Szot, and R. Waser, "Piezoresponse Force Microscopy of Lead Titanate Nanograins Possibly Reaching the Limit of Ferroelectricity," *Appl. Phys. Lett.*, **81**, 5231–3 (2002).
[99]A. Roelofs, "Size Effects in Ferroelectric Thin Films," Ph.D. Thesis, RTWH Aachen, Germany, 2004.
[100]A. L. Kholkin, V. V. Shvartsman, A. Yu. Emelyanov, R. Poyato, M. L. Calzada, and L. Pardo, "Stress-Induced Suppression of Piezoelectric Properties in $PbTiO_3$:La Thin Films Via Scanning Force Microscopy," *Appl. Phys. Lett.*, **82**, 2127–9 (2002).
[101]M. Abplanalp, J. Fousek, and P. Günter, "Higher Order Ferroic Switching Induced by Scanning Force Microscopy," *Phys. Rev. Lett.*, **86**, 5799–802 (2001).
[102]M. Labardi, C. Polop, V. Likodimos, L. Pardi, M. Allegrini, E. Vasco, and C. Zaldo, "Surface Deformation and Ferroelectric Domain Switching Induced by a Force Microscope Tip on a La-Modified $PbTiO_3$ Thin Film," *Appl. Phys. Lett.*, **83**, 2028–30 (2003).
[103]A. Gruverman, Private Communications.
[104]M. Alexe, A. Gruverman, C. Harnagea, N. D. Zakharov, A. Pignolet, D. Hesse, and J. F. Scott, "Switching Properties of Self-Assembled Ferroelectric Memory Cells," *Appl. Phys. Lett.*, **75**, 1158–60 (1999).
[105]S. V. Kalinin, A. Gruverman, and D. A. Bonnell, "Quantitative Analysis of Nanoscale Switching in $SrBi_2Ta_2O_9$ Thin Films by Piezoresponse Force Microscopy," *Appl. Phys. Lett.*, **85**, 795–8 (2004).
[106]R. Shao and D. A. Bonnell, "Scanning Probes of Nonlinear Properties in Complex Materials," *Jpn. J. Appl. Phys.*, **43**, 4471–6 (2004).
[107]Q. M. Zhang, W. Y. Pan, and L. E. Cross, "Laser Interferometer for the Study of Piezoelectric and Electrostrictive Strains," *J. Appl. Phys.*, **63**, 2492–4 (1988).
[108]I. L. Guy and Z. Zheng, "Piezoelectricity and Electrostriction in Ferroelectric Polymers," *Ferroelectrics*, **264** [1–4] 1691–6 (2001).
[109]T. Furukawa and N. Seo, "Electrostriction as the Origin of Piezoelectricity in Ferroelectric Polymer," *Jpn. J. Appl. Phys.*, **29**, 675–80 (1990).
[110]C. Gao and X. D. Xiang, "Quantitative Microwave Near-Field Microscopy of Dielectric Properties," *Rev. Sci. Instrum.*, **69**, 3846–51 (1998).
[111]Y. Cho, A. Kirihara, and T. Saeki, "Scanning Nonlinear Dielectric Microscope," *Rev. Sci. Instrum.*, **67**, 2297–303 (1996).
[112]D. E. Steinhauer, C. P. Vlahacos, F. C. Wellstood, S. M. Anlage, C. Canedy, R. Ramesh, A. Stanishevsky, and J. Melngailis, "Imaging of Microwave Permittivity, Tunability, and Damage Recovery in (Ba, Sr)TiO_3 Thin Films," *Appl. Phys. Lett.*, **75**, 3180–2 (1999).
[113]D. E. Steinhauer, C. P. Vlahacos, S. K. Dutta, F. C. Wellstood, and S. M. Anlage, "Surface Resistance Imaging with a Scanning Near-Field Microwave Microscope," *Appl. Phys. Lett.*, **71**, 1736–8 (1997).
[114]S. C. Lee and S. M. Anlage, "Spatially-Resolved Nonlinearity Measurements of $YBa_2Cu_3O_{7-\delta}$ Bicrystal Grain Boundaries," *Appl. Phys. Lett.*, **82**, 1893–5 (2003).
[115]L. M. Levinson (ed.), *Electronic Ceramics: Properties, Devices and Applications*. Marcel Dekker Inc., New York, 1988.
[116]D. R. Clarke, "On the Detection of Thin Intergranular Films by Electron Microscopy," *Ultramicroscopy*, **4**, 33–44 (1979).
[117]Y.-M. Chiang, W. D. Kingery, and L. M. Levinson, "Compositional Changes Adjacent to Grain Boundaries During Electrical Degradation of a ZnO Varistor," **53**, 1765–8 (1982).
[118]S. B. Desu and D. A. Payne, "Interfacial Segregation in Perovskites. I. Theory," *J. Am. Ceram. Soc.*, **73**, 3391–7 (1990).
[119]J. A. S. Ikeda and Y.-M. Chiang, "Space Charge Segregation at Grain Boundaries in Titanium Dioxide: I, Relationship Between Lattice Defect Chemistry and Space Charge Potential," *J. Am. Ceram. Soc.*, **76**, 2437–46 (1993).
[120]J. D. Russell, D. C. Halls, and C. Leach, "The Relationship Between Crystal Misorientation and Conductive Mode Contrast of Grain Boundaries in Additive-Free Zinc Oxide," *J. Mater. Sci.*, **32**, 4585–9 (1997).
[121]Z. Ling, "A REBIC and CL Study of Interfaces in a Zinc Oxide Based Varistor," *J. Mater. Sci.*, **34**, 6133–5 (1999).
[122]J. Fleig, S. Rodewald, and J. Maier, "Spatially Resolved Measurements of Highly Conductive and Highly Resistive Grain Boundaries Using Microcontact Impedance Spectroscopy," *Sol. State Ionics*, **136–137**, 905–911 (2000).
[123]G. E. Pike and C. H. Seager, "The dc Voltage Dependence of Semiconductor Grain-Boundary Resistance," *J. Appl. Phys.*, **50**, 3414–22 (1979).
[124]R. A. De Souza, J. Fleig, J. Maier, O. Kienzle, Z. Zhang, W. Sigle, and M. Rühle, "Electrical and Structural Characterization of a Low-Angle Tilt Grain Boundary in Iron-Doped Strontium Titanate," *J. Am. Ceram. Soc.*, **86**, 922–8 (2003).
[125]Z. Zhang, W. Sigle, W. Kurtz, and M. Rühle, "Electronic and Atomic Structure of a Dissociated Dislocation in $SrTiO_3$," *Phys. Rev. B*, **66**, 214112 (2002).
[126]F. Ernst, O. Kienzle, and M. Rühle, "Structure and Composition of Grain Boundaries in Ceramics," *J. Eur. Ceram. Soc.*, **19**, 665–73 (1999).
[127]M. Kim, G. Duscher, N. D. Browning, K. Sohlberg, S. T. Pantelides, and S. J. Pennycook, "Nonstoichiometry and the Electrical Activity of Grain Boundaries in $SrTiO_3$," *Phys. Rev. Lett.*, **86**, 4056–9 (2001).
[128]N. D. Browning and S. J. Pennycook, "Direct Experimental Determination of the Atomic Structure at Internal Interfaces," *J. Phys.*, **D 29**, 1779–98 (1996).
[129]K. D. Johnson and V. P. Dravid, "Grain Boundary Barrier Breakdown in Niobium Donor Doped Strontium Titanate Using In Situ Electron Holography," *Appl. Phys. Lett.*, **74**, 621–3 (1999).
[130]N. D. Browning, J. P. Buban, H. O. Moltaji, S. J. Pennycook, G. Duscher, K. D. Johnson, R. P. Rodrigues, and V. P. Dravid, "The Influence of Atomic Structure on the Formation of Electrical Barriers at Grain Boundaries in $SrTiO_3$," *Appl. Phys. Lett.*, **74**, 2638–40 (1999).
[131]S. V. Kalinin and D. A. Bonnell, "Surface Potential at Surface–Interface Junctions in $SrTiO_3$ Bicrystals," *Phys. Rev. B*, **62**, 10419–30 (2000).
[132]V. Ravikumar, R. P. Rodrigues, and V. P. Dravid, "Direct Imaging of Spatially Varying Potential and Charge Across Internal Interfaces in Solids," *Phys. Rev. Lett.*, **75**, 4063–6 (1995).

[133]Z. Mao, R. E. Dunin-Borkowski, G. B. Boothroyd, and K. M. Knowles, "Direct Measurement and Interpretation of Electrostatic Potentials at 24° [001] Tilt Boundaries in Undoped and Niobium-Doped Strontium Titanate Bicrystals," *J. Am. Ceram. Soc.*, **81**, 2917–43 (1998).
[134]V. Ravikumar, R. P. Rodrigues, and V. P. Dravid, "An Investigation of Acceptor-Doped Grain Boundaries in $SrTiO_3$," *J. Phys.*, **D 29**, 1799–806 (1996).
[135]M. M. McGibbon, N. D. Browning, A. J. McGibbon, and S. J. Pennycook, "The Atomic Structure of Asymmetric [001] Tilt Boundaries in $SrTiO_3$," *Phil. Mag.*, **A 73**, 625 (1996).
[136]N. D. Browning, H. O. Moltaji, and J. P. Buban, "Investigation of Three-Dimensional Grain-Boundary Structures in Oxides Through Multiple-Scattering Analysis of Spatially Resolved Electron-Energy-Loss Spectra," *Phys. Rev. B*, **58**, 8289 (1998).
[137]G. Duscher, J. P. Buban, N. D. Browning, M. F. Chisholm, and S. J. Pennycook, "The Electronic Structure of Pristine and Doped (100) Tilt Grain Boundaries in $SrTiO_3$," *Interf. Sci.*, **8**, 199–208 (2000).
[138]S.-D. Mo, W. Y. Ching, M. F. Chisholm, and G. Duscher, "Electronic Structure of a Grain-Boundary Model in $SrTiO_3$," *Phys. Rev. B*, **60**, 2416–24 (1999).
[139]R. Astala and P. D. Bristowe, "First-Principles Calculations of an Oxygen Deficient Σ3 (111) [101] Grain Boundary in Strontium Titanate," *J. Phys.: Condens. Matter*, **14**, 6455–67 (2002).
[140]Z. Zhang, W. Sigle, and M. Rühle, "Atomic and Electronic Characterization of the a [100] Dislocation Core in $SrTiO_3$," *Phys. Rev. B*, **66**, 94108 (2002).
[141]Z. Zhang, W. Sigle, F. Phillips, and M. Rühle, "Direct Atom-Resolved Imaging of Oxides and Their Grain Boundaries," *Science*, **302**, 846–9 (2003).
[142]E. McDaniel, S. McClain, and J. W. P. Hsu, "Nanometer Scale Polarimetry Studies Using a Near Field Optical Microscope," *Appl. Opt.*, **37**, 84–92 (1998).
[143]E. McDaniel and J. W. P. Hsu, "Direct Imaging of Submicron Scale Defect Induced Birefringence in $SrTiO_3$ Bicrystals," *J. Appl. Phys.*, **84**, 189–93 (1998).
[144]D. A. Bonnell and S. V. Kalinin, "Non-Linear Dielectric Properties at Oxide Grain Boundaries," *Z. Metallkd.*, **94**, 188–94 (2003).
[145]R. Shao and D. A. Bonnell, unpublished.
[146]J. Petzelt, T. Ostapchuk, and I. Gregora *et al.*, "Dielectric, Infrared, and Raman Response of Undoped $SrTiO_3$ Ceramics: Evidence of Polar Grain Boundaries," *Phys. Rev. B*, **64**, 184111 (2001).
[147]S. V. Kalinin and D. A. Bonnell, "Screening Phenomena on Oxide Surfaces and its Implications for Local Electrostatic and Transport Measurements," *Nano Lett.*, **4**, 555–60 (2004).
[148]R. Shao and D. A. Bonnell, Unpublished.
[149]M. E. Lines, and A. M. Glass (eds.), *Principles and Applications of Ferroelectric and Related Materials*. Clarendon Press, Oxford, 1977.
[150]L. L. Hench and J. K. West (eds.), *Principles of Electronic Ceramics*. Wiley, New York, 1990.
[151]N. Setter and E. L. Colla (eds.), *Ferroelectric Ceramics*. Birkhauser Verlag, Basel, 1993.
[152]D. L. Polla and L. F. Francis, "Processing and Characterization of Piezoelectric Materials and Integration into Microelectromechanical Systems," *Annu. Rev. Mater. Sci.*, **28**, 563–97 (1998).
[153]D. M. Dabbs and I. A. Aksay, "Self-Assembled Ceramics Produced by Complex-Fluid Templation," *Annu. Rev. Phys. Chem.*, **51**, 601–22 (2000).
[154]U. P. Schonholzer and L. J. Gauckler, "Ceramic Parts Patterned in the Micrometer Range," *Adv. Mater.*, **11**, 630–2 (1999).
[155]V. R. Palkar, S. C. Purandare, and R. Pinto, "Ferroelectric Thin Films of $PbTiO_3$ on Silicon," *J. Phys.*, **D 32**, R1–18 (1999).
[156]M. Suzuki, "Review on Future Ferroelectric Nonvolatile Memory: FeRAM from the Point of View of Epitaxial Oxide Thin Films," *J. Ceram. Soc. Jpn.*, **103**, 1099–111 (1995).
[157]J. Scott, *Ferroelectric Memories*. Springer Verlag, Berlin, 2000.
[158]J. S. Speck and W. Pompe, "Domain Configurations Due to Multiple Misfit Relaxation Mechanisms in Epitaxial Ferroelectric Thin Films. I. Theory," *J. Appl. Phys.*, **76**, 466–76 (1994).
[159]J. S. Speck, A. Seifert, W. Pompe, and R. Ramesh, "Domain Configurations Due to Multiple Misfit Relaxation Mechanisms in Epitaxial Ferroelectric Thin Films. II. Experimental Verification and Implications," *J. Appl. Phys.*, **76**, 477–83 (1994).
[160]V. Nagarajan, I. G. Jenkins, S. P. Alpay, H. Li, S. Aggarwal, L. Salamanca-Riba, A. L. Roytburd, and R. Ramesh, "Thickness Dependence of Structural and Electrical Properties in Epitaxial Lead Zirconate Titanate Films," *J. Appl. Phys.*, **86**, 595–602 (1999).
[161]Y. L. Li, S. Y. Hu, Z. K. Liu, and L. Q. Chen, "Effect of Substrate Constraint on the Stability and Evolution of Ferroelectric Domain Structures in Thin Films," *Acta Mater.*, **50**, 395–411 (2002).
[162]F. Jona and G. Shirane, *Ferroelectric Crystals*. Dover Publications, New York, 1993.
[163]G. A. Smolenskii, V. A. Bokov, V. A. Isupov, N. N. Krainik, R. E. Pasynkov, and A. I. Sokolov, *Ferroelectrics and Related Materials*. Gordon and Breach, New York, 1984.
[164]B. Jaffe, W. R. Cook Jr., and H. Jaffe, *Piezoelectric Ceramics*. Academic Press, London, 1971.
[165]M. L. Mulvihill, K. Uchino, Z. Li, and W. Cao, "In-Situ Observation of the Domain Configurations During the Phase Transitions in Barium Titanate," *Philos. Mag.*, **B 74**, 25–36 (1996).
[166]V. Gopalan, Q. X. Jia, and T. E. Mitchell, "*In situ* Video Observation of 180° Domain Kinetics in Congruent $LiNbO_3$ Crystals," *Appl. Phys. Lett.*, **75**, 2482–4 (1999).
[167]S. Zhu and W. Cao, "Imaging of 180° Ferroelectric Domains in $LiTaO_3$ by Means of Scanning Electron Microscopy," *Phys. Stat. Sol.*, **A 173**, 495–503 (1999).
[168]A. A. Sogr, "Domain Structure of Ferroelectrics Observed in the Scanning Electron Microscope," *Ferroelectrics*, **97**, 47–57 (1989).
[169]I. M. Reaney, "TEM Observations of Domains in Ferroelectric and Nonferroelectric Perovskites," *Ferroelectrics*, **172**, 115–25 (1995).
[170]L. A. Bursill and P. J. Lin, "Electron Microscopic Studies of Ferroelectric Crystals," *Ferroelectrics*, **70**, 191–203 (1986).
[171]E. Snoeck, L. Normand, A. Thorel, and C. Roucau, "Electron Microscopy Study of Ferroelastic and Ferroelectric Domain Wall Motions Induced by the In Situ Application of an Electric Field in $BaTiO_3$," *Phase Transitions*, **46**, 77–88 (1994).
[172]Z. Xu, D. Viehland, P. Yang, and D. A. Payne, "Hot-Stage Transmission Electron Microscopy Studies of Phase Transformations in Tin-Modified Lead Zirconate Titanate," *J. Appl. Phys.*, **74**, 3406–13 (1993).
[173]O. O. Popoola and W. M. Kriven, "Is the Hagen-Strunk Multiplication Mechanism of Misfit Dislocations in Heteroepitaxial Layers Probable?," *Philos. Mag. Lett.*, **75**, 1–8 (1997).
[174]E. Snoeck, C. Roucau, P. Baules, M. J. Casanove, M. Fagot, B. Astie, and J. Degauque, "Use of In Situ TEM Experiments for Phase Transition Studies," *Microsc., Microanal., Microstruct.*, **4**, 249–64 (1993).
[175]N. Yamamoto, K. Yagi, and G. Honjo, "Electron Microscopic Studies of Ferroelectric and Ferroelastic Gadolinium Molybdate ($Gd_2(MoO_4)_3$). IV. Polarization Reversal and Field Induced Phase Transformation," *Phys. Stat. Sol.*, **A 62**, 657–64 (1980).
[176]H. Riege, I. Boscolo, J. Handerek, and U. Herleb, "Features and Technology of Ferroelectric Electron Emission," *J. Appl. Phys.*, **84**, 1602–17 (1998).
[177]D. Shur and G. Rosenman, "Figures of Merit for Ferroelectric Electron Emission Cathodes," *J. Appl. Phys.*, **80**, 3445–50 (1996).
[178]W.-C. Yang, B. J. Rodriguez, A. Gruverman, and R. J. Nemanich, "Polarization-Dependent Electron Affinity of $LiNbO_3$ Surfaces," *Appl. Phys. Lett.*, **85**, 2316–8 (2004).
[179]J. L. Giocondi and G. S. Rohrer, "Spatially Selective Photochemical Reduction of Silver on the Surface of Ferroelectric Barium Titanate," *Chem. Mater.*, **13** [2] 241–2 (2001).
[180]S. V. Kalinin, D. A. Bonnell, T. Alvarez, X. Lei, Z. Hu, J. H. Ferris, Q. Zhang, and S. Dunn, "Atomic Polarization and Local Reactivity on Ferroelectric Surfaces: A New Route Toward Complex Nanostructures," *Nano Lett.*, **2** [6] 589–93 (2002).
[181]S. V. Kalinin, D. A. Bonnell, T. Alvarez, X. Lei, Z. Hu, R. Shao, and J. H. Ferris, "Ferroelectric Lithography of Multi Component Nanostructures," *Adv. Mater.*, **16**, 795–9 (2004).
[182]V. M. Fridkin, *Ferroelectric Semiconductors*. Consultants Bureau, New York, 1980.
[183]C. H. Ahn, S. Gariglio, P. Paruch, T. Tybell, L. Antognazza, and J.-M. Triscone, "Electrostatic Modulation of Superconductivity in Ultrathin $GdBa_2Cu_3O_{7-x}$ Films," *Science*, **284**, 1152–5 (1999).
[184]C. H. Ahn, T. Tybell, L. Antognazza, K. Char, R. H. Hammond, M. R. Beasley, O. Fischer, and J.-M. Triscone, "Local, Nonvolatile Electronic Writing of Epitaxial $Pb(Zr_{0.52}Ti_{0.48})O_3/SrRuO_3$ Heterostructures," *Science*, **276**, 1100–3 (1997).
[185]Y. G. Wang, J. Dec, and W. Kleemann, "Study on Surface and Domain Structures of $PbTiO_3$ Crystals by Atomic Force Microscopy," *J. Appl. Phys.*, **84**, 6795–9 (1998).
[186]A. L. Gruverman, J. Hatano, and H. Tokumoto, "Scanning Force Microscopy Studies of Domain Structure in $BaTiO_3$ Single Crystals," *Jpn. J. Appl. Phys.*, **A 36**, 2207–11 (1997).
[187]M. Takashige, S.-I. Hamazaki, N. Fukurai, F. Shimizu, and S. Kojima, "Atomic Force Microscope Observation of Ferroelectrics: Barium Titanate and Rochelle Salt," *Jpn. J. Appl. Phys.*, **B 35**, 5181–4 (1996).
[188]M. Takashige, S.-I. Hamazaki, F. Shimizu, and S. Kojima, "Temperature Dependent Surface Images of Barium Titanate and Rochelle Salt Observed by Atomic Force Microscopy," *Ferroelectrics*, **240**, 1359–66 (2000).
[189]S. Balakumar, J. B. Xu, J. X. Ma, S. Ganesamoorthy, and I. H. Wilson, "Surface Morphology of Ferroelectric Domains in BaTiO3 Single Crystals: An Atomic Force Microscope Study," *Jpn. J. Appl. Phys.*, **A 36**, 5566–9 (1997).
[190]G. K. H. Pang and K. Z. Baba-Kishi, "Characterization of Butterfly Single Crystals of $BaTiO_3$ by Atomic Force, Optical and Scanning Electron Microscopy Techniques," *J. Phys.*, **D 31**, 2846–53 (1998).
[191]L. M. Eng, M. Friedrich, J. Fousek, and P. Günter, "Deconvolution of Topographic and Ferroelectric Contrast by Noncontact and Friction Force Microscopy," *J. Vac. Sci. Technol.*, **B 14**, 1191–6 (1996).
[192]H. Bluhm, U. D. Schwartz, and R. Wiesendanger, "Origin of the Ferroelectric Domain Contrast Observed in Lateral Force Microscopy," *Phys. Rev. B*, **57**, 161–9 (1998).
[193]A. Correia, J. Massanell, N. Garcia, A. P. Levanyuk, A. Zlatkin, and J. Przeslawski, "Friction Force Microscopy Study of a Cleaved Ferroelectric Surface: Time and Temperature Dependence of the Contrast, Evidence of Domain Structure Branching," *Appl. Phys. Lett.*, **68**, 2796–8 (1996).
[194]R. Lüthi, H. Haefke, K.-P. Meyer, E. Meyer, L. Howald, and H.-J. Güntherodt, "Surface and Domain Structures of Ferroelectric Crystals Studied with Scanning Force Microscopy," *J. Appl. Phys.*, **74**, 7461–71 (1993).
[195]R. Lüthi, H. Haefke, W. Gutmannsbauer, E. Meyer, L. Howald, and H.-J. Güntherodt, "Statics and Dynamics of Ferroelectric Domains Studied with Scanning Force Microscopy," *J. Vac. Sci. Technol.*, **B 12**, 2451–5 (1996).
[196]F. Saurenbach and B. D. Terris, "Imaging of Ferroelectric Domain Walls by Force Microscopy," *Appl. Phys. Lett.*, **56**, 1703–5 (1990).
[197]J. Ohgami, Y. Sugawara, S. Morita, E. Nakamura, and T. Ozaki, "Determination of Sign of Surface Charges of Ferroelectric TGS Using Electrostatic

Force Microscope Combined with the Voltage Modulation Technique," *Jpn. J. Appl. Phys.*, **A 35**, 2734–9 (1996).
[198]L. M. Eng, J. Fousek, and P. Günter, "Ferroelectric Domains and Domain Boundaries Observed by Scanning Force Microscopy," *Ferroelectrics*, **191**, 211–8 (1997).
[199]S. V. Kalinin and D. A. Bonnell, "Electric Scanning Probe Imaging and Modification of Ferroelectric Surfaces;" pp. 1–43 in *Nanoscale Characterization of Ferroelectric Materials*, Edited by M. Alexe and A. Gruverman. Springer, Berlin, Germany, 2004.
[200]E. Z. Luo, Z. Xie, J. B. Xu, I. H. Wilson, and L. H. Zhao, "In Situ Observation of the Ferroelectric–Paraelectric Phase Transition in a Triglycine Sulfate Single Crystal by Variable-Temperature Electrostatic Force Microscopy," *Phys. Rev. B*, **61**, 203–6 (2000).
[201]J. W. Hong, S. I. Park, and Z. G. Kim, "Measurement of Hardness, Surface Potential, and Charge Distribution with Dynamic Contact Mode Electrostatic Force Microscope," *Rev. Sci. Instrum.*, **70**, 1735–9 (1999).
[202]L. M. Eng, H. J. Güntherodt, G. Rosenman, A. Skliar, M. Oron, M. Katz, and D. Eger, "Nondestructive Imaging and Characterization of Ferroelectric Domains in Periodically Poled Crystals," *J. Appl. Phys.*, **83**, 5973–7 (1998).
[203]V. Likodimos, X. K. Orlik, L. Pardi, M. Labardi, and M. Allegrini, "Dynamical Studies of the Ferroelectric Domain Structure in Triglycine Sulfate by Voltage-Modulated Scanning Force Microscopy," *J. Appl. Phys.*, **87**, 443–51 (2000).
[204]A. Y. Borisevich, S. V. Kalinin, D. A. Bonnell, and P. K. Davies, "Analysis of Phase Distributions in the Li_2O–Nb_2O_5–TiO_2 System by Piezoresponse Imaging," *J. Mater. Res.*, **16**, 329–32 (2001).
[205]T. Tybell, C. H. Ahn, and J.-M. Triscone, "Ferroelectricity in Thin Perovskite Films," *Appl. Phys. Lett.*, **75**, 856–8 (1999).
[206]X. K. Orlik, V. Likodimos, L. Pardi, M. Labardi, and M. Allegrini, "Scanning Force Microscopy Study of the Ferroelectric Phase Transition in Triglycine Sulfate," *Appl. Phys. Lett.*, **76**, 1321–4 (2000).
[207]V. Likodimos, M. Labardi, and M. Allegrini, "Domain Pattern Formation and Kinetics on Ferroelectric Surfaces Under Thermal Cycling Using Scanning Force Microscopy," *Phys. Rev. B*, **66**, 024104 (2002).
[208]V. Nagarajan, A. Roytburd, A. Stanishevsky, S. Prasertchoung, T. Zhao, L. Chen, J. Melngailis, O. Auciello, and R. Ramesh, "Dynamics of Ferroelastic Domains in Ferroelectric Thin Films," *Nature Mater.*, **2**, 43–7 (2003).
[209]E. L. Colla, S. Hong, D. V. Taylor, A. K. Tagantsev, N. Setter, and K. No, "Direct Observation of Region by Region Suppression of the Switchable Polarization (Fatigue) in $Pb(Zr,Ti)O_3$ Thin Film Capacitors with Pt Electrodes," *Appl. Phys. Lett.*, **72**, 2763–6 (1998).
[210]S. Hong, "Polarization Switching and Fatigue of Ferroelectric Thin Films Studied by PFM;" pp. 111–35 in *Nanoscale Phenomena in Ferroelectric Thin Films*, Edited by S. Hong. Kluwer, Dordrecht, 2004. □

Sergei Kalinin is currently a research staff member at the Oak Ridge National Laboratory. He completed his Ph.D. in Materials Science at the University of Pennsylvania. His previous undergraduate and graduate work was completed in Materials Science at Moscow State University, Moscow, Russia. His current research interests include synthesis and characterization of electronic, transport and magnetic phenomena in transition metal oxides on the nanoscale. The special emphasis of his research is on the development and quantitative interpretation of scanning probe microscopy techniques, including piezoresponse force microscopy, Kelvin probe force microscopy and SPM based transport and conductivity measurements. During his academic career, Sergei has been the recipient of the Ross Coffin Purdy Award of American Ceramics Society for the development of Scanning Impedance Microscopy, a novel SPM technique for the characterization of ac transport on the nanoscale. He is also a recipient of Wigner Fellowship of Oak Ridge National Laboratory. As a student, he earned multiple research awards including AVS Graduate Student Award and several Materials Research Society Graduate Student Awards. He is the author of more than 60 scientific papers, eight books and book chapters on electrical SPM techniques, and several patents.

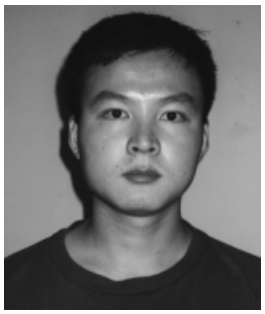

Mr. Rui Shao received his B. S. (2000) degree in Physics from the University of Science and Technology of China. He is currently a Ph.D. student in Materials Science at the University of Pennsylvania. His research interests are in oxide thin films, and scanning probe characterization of electrical properties and atomic structures of oxide grain boundaries.

Dawn Bonnell is the Trustee Professor of Materials Science at the University of Pennsylvania and the Director of the Nano/Bio Interface Center. She received her PhD from the University of Michigan and was a Fulbright scholar to the Max-Planck-Institute in Stuttgart, Germany, after which she worked at IBM Thomas Watson Research Center. Her current research involves atomistic processes at oxide surfaces, nanometer scale electronic phenomena in materials, and assembly of complex nanostructures. She has authored or coauthored over 180 papers, edited several books, including *Scanning Probe Microscopy and Spectroscopy: theory, techniques, and applications.* Her work has been recognized by the Presidential Young Investigators Award, the Ross Coffin Purdy Award, and several distinguished lectureships. Professor Bonnell has taught short courses for scientific societies, served as a Founding Board member of the Nanoscale Science and Technology Division of AVS, and is a president of AVS. She has served in leadership positions in the Basic Science Division and Exhibitions and Meetings Committee, and is a fellow of the American Ceramic Society. She serves on the editorial boards of several journals, on national and international advisory committees, and is involved with several nanotechnology based companies.